Galactic Cosmic Rays, Cosmic-Ray Variations, and Cosmogenic Nuclides in Meteorites

Ingo Leya[1] , Jason Hirtz[1,2], and Jean-Christophe David[2]
[1] Physics Institute, University of Bern, Sidlerstrasse 5, 3012 Bern, Switzerland; ingo.leya@space.unibe.ch
[2] CEA/Saclay, Irfu/DPhN, F-91191 Gif-sur-Yvette, Cedex, France
Received 2020 December 1; revised 2021 February 8; accepted 2021 February 9; published 2021 April 5

Abstract

We present a new generation of model calculations for cosmogenic production rates in various types of solar system bodies. The model is based on the spectra for primary and secondary particles calculated using the INCL++6 code, which is the most reliable and most sophisticated code available for spallation reactions. Thanks to the recent improvements (extending the code to lower and higher energies and considering light charged particles as ejectiles and projectiles), we can for the first time directly consider primary and secondary Galactic α particles. We calculate production rates for ^{22}Na, ^{10}Be, and ^{26}Al in an L-chondrite with a radius of 45 cm and in the Apollo 15 drill core, and we determine the long-term average Galactic cosmic-ray (GCR) spectrum (represented by the solar modulation potential Φ) in the meteoroid orbits at $\sim$3 au of $\Phi = 600$ MV and at 1 au, i.e., for Earth and Moon of $\Phi = 660$ MV. From this, we calculate a long-term average GCR gradient in the inner solar system of $\sim$5% au^{-1}. Finally, we discuss the possibility of studying temporal GCR variations and meteoroid orbits using production rate ratios of short- and long-lived radionuclides.

Unified Astronomy Thesaurus concepts: Galactic cosmic rays (567); Meteorites (1038); Heliosphere (711); The Moon (1692)

1. Introduction

The detection and the study of Galactic cosmic rays (GCRs) started with the balloon flights by V. Hess (Hess 1912). With the balloon flights, he demonstrated (i) a slight increase of the atmospheric ionization with increasing altitude and (ii) that the Sun could not be the reason for the hypothetical new radiation. Already in 1913, the finding by Hess was fully confirmed by Kohlhörster (1913), who finally reached altitudes of 9300 m (Kohlhörster 1914). That the Sun was not the source of the newly found cosmic rays was apparent already after the first pioneering study, because there was no intensity difference (measured by the discharge rate of an electroscope) between day-time and night-time measurements (Hess 1912). Interestingly, that supernovae are likely sources of the cosmic rays was suspected relatively early by Baade & Zwicky (1934a, 1934b, 1934c). Note that supernova remnants are still considered likely sources for cosmic rays with energies less than $\sim10^{16}$ eV. At higher energies, particularly above 10^{18} eV, where the particles are almost certainly extragalactic, the origin is still a matter of debate. A recent review on the early history of cosmic particle physics can be found in Walter & Wolfendale (2012).

While the study of GCRs is a very interesting topic in itself, especially after the two Voyager missions left the heliosphere, the focus is very often on the interactions between GCR particles with meteorites, the lunar surface, the terrestrial atmosphere, terrestrial surface samples, and other solar system objects. Our goal is, on the one hand, to better understand and quantify the physical processes of nuclide production and, on the other hand, to use the results to better understand the dynamics of small bodies in the solar system. In addition, we always try to find ways of using nuclide production in other, so far less-explored research fields, e.g., early solar system irradiation scenarios, erosion rates, and others. For a recent review, see, e.g., David & Leya (2019).

In recent years, the combination of Monte Carlo calculations for the primary and secondary particle fluxes in the irradiated objects and the cross sections for the relevant nuclear reactions has been demonstrated to be relatively successful in calculating the various cosmic-ray effects in solar system bodies. Over the years, there have been groups using this approach to study cosmogenic nuclide production in Earth's atmosphere (e.g., Masarik & Beer 1999), in terrestrial surface samples (e.g., Argento et al. 2015a, 2015b), in the lunar surface (e.g., McKinney et al. 2006; Kim et al. 2010; Li et al. 2017), and in meteorites (e.g., Masarik & Reedy 1996; Ammon et al. 2008; Leya & Masarik 2009; Kim et al. 2010). However, so far, there is no model that has consistently been applied in a large variety of different solar system objects. Our goal is to establish such a model, i.e., a model that is able to consistently and reliably describe all aspects of cosmogenic nuclide production by solar and GCRs in all possible types of solar system bodies, from tiny dust grains, to planetary surfaces, and finally also to exoplanetary atmospheres.

Considering that the intranuclear cascade is the dominant part for any Monte Carlo model calculating particle spectra in irradiated bodies, the quality of the model calculations for cosmogenic production rates directly depends on the quality with which the intranuclear cascade is calculated. In this respect, the recent impressive improvements achieved for spallation models, i.e., for models describing the intranuclear cascade part of a high-energy nuclear reaction, are important. Here we focus on the Liège Intranuclear Cascade Model INCL, which is one of the best codes available, especially when coupled to ABLA, a code that describes the de-excitation part of a spallation reaction (e.g., Leray et al. 2013). In recent years, the INCL–ABLA combination has been significantly and successfully extended with respect to (i) light-charged-particle-induced reactions, (ii) ejection of light charged particles up to $z = 8$, and (iii) extending the applicability of the code to lower energies in the range of a few MeV. For more information and a summary, see, e.g., Leray et al. (2013) and David (2015). In a recent project, we further updated the code by improving its applicability to higher energies, i.e., to energies in the range of

20 GeV, by adding strange particles to the system (Hirtz et al. 2018, 2020; Hirtz 2019). It is safe to conclude that INCL++6, how the code is called now, is currently the most sophisticated, accurate, and reliable code for modeling the intranuclear cascade part of a nuclear reaction. Now is a good time to establish a new reliable and consistent model for cosmogenic production rates.

We discuss in Section 2 in some detail the particle spectra used for modeling, starting with the different approaches that can be in found in the literature for the local interstellar spectrum (LIS), summarizing the various aspects of particle modulation in the heliosphere, and finally discussing GCR gradients in the inner solar system. In Section 3, we briefly present our new model for cosmogenic production rates, called CosmicTransmutation. More information can be found in Hirtz (2019). In Section 4, our best estimates for the long-term average GCR spectrum in the meteoroid orbits at $\sim$3 au and at an orbital distance of 1 au are given. From this result, we discuss the long-term average GCR gradient in the inner solar system. Finally, we use the ^{10}Be, ^{26}Al, and ^{22}Na production rates in meteorites and the Moon to study (i) if cosmogenic production rate ratios can be used to determine temporal GCR intensity variations (if the orbit is known) and (ii) if the ^{22}Na/^{26}Al production rate ratio can be used to put constraints on the final part of the meteoroid orbit if the GCR spectrum and the radial gradient are both independently known (Section 5.2).

Though the CosmicTransmutation model is able to calculate cosmic-ray effects in all types of solar system bodies, we focus here on meteorites and the Moon, which are well-studied objects and which are therefore perfectly suited to evaluate the model predictions. Studies of other solar system objects are planned and some of them have already been started.

2. Galactic Cosmic Rays

GCRs are energetic particles that originate from outside the solar system. They consist of $\sim$87% protons, $\sim$12% helium nuclei, and $\sim$1% heavier ions (the exact composition depends on the energy). The energy spectra for all particle types are similar if displayed as a function of energy per nucleon (Simpson 1983). According to the standard model for the origin and propagation of GCRs, they are accelerated in the waves of supernova explosions and propagate diffusively through the galaxy, interacting with the interstellar gas (e.g., Amato & Blasi 2018). This acceleration process also collects particles from the interstellar medium (ISM) and hence the mass composition of the GCRs is expected to reflect the composition of the ISM. All recent studies and missions clearly support models of diffusive shock acceleration of GCR protons interacting with the molecular gas. In such models, 12%–16% of the total energy of the supernova ejecta is available for cosmic-ray acceleration. Candidates for efficient GCR production and acceleration are so-called superbubbles, e.g., many stars that go supernovae in a short time frame of only a few Myr in clusters of only a few parsecs in diameter. For more information, see, e.g., Binns et al. (2008) and Lingenfelter (2018).

Outside the solar system, the GCR flux can (roughly) be regarded as isotropic and time independent (the latter might not be true; see below). When entering the heliosphere, which is in the region of $\sim$200 au, the GCR particles encounter the turbulent solar wind and the magnetic field embedded in the wind. Because both vary with time and space, the GCR flux in

the heliosphere is a function of radial distance and time. This process is known as the solar modulation of cosmic rays (see also Section 2.2).

Recent data from PAMELA, CREAM, and AMS-2 have shown that the GCR particle spectrum, which was often considered featureless, is actually rich in structures. An interesting example is that the spectra of protons and helium nuclei seem to flatten in the energy range of 200–300 GeV nucleon^{-1}. The slopes of the different GCR species are slightly different from each other, which leads to the dominance of the helium flux over the hydrogen flux at energies higher than 100 TeV. For a recent review of some of the new and interesting findings, see Amato & Blasi (2018).

2.1. The Local Interstellar Proton Spectrum

One of the most important ingredients for any study of GCRs and cosmogenic nuclides is the LIS, i.e., the Galactic particle spectrum outside the heliosphere. For relatively low energies, i.e., a few hundred MeV nucleon^{-1}, there are data from the two Voyager missions. In 2012 August, Voyager 1 crossed the heliopause at $\sim$122 au and entered the local ISM in the northern hemisphere. There, the GCR flux abruptly reached a higher interstellar level (factor of $\sim$1.5 compared to the values in the heliosphere) and then essentially remained constant (e.g., Webber & McDonald 2013). However, the GCR intensity immediately beyond the heliosphere might be lower than the intensity of the LIS because of some remaining modulation (Stone et al. 2013, 2019). Further beyond, the modulation of cosmic rays does not depend on the magnetic field configuration outside the heliopause (Zhang & Pogorelov 2000; Webber & McDonald 2013). In 2018 December, Voyager 2 crossed the heliopause (also at $\sim$120 au) essentially confirming the results from Voyager 1. The energy spectra for all measured particles are nearly identical for Voyager 1 and Voyager 2 despite both spacecraft being separated by $\sim$167 au. This indicates that there is no significant intensity gradient of the particle fluxes in this region of the local ISM, at least not for the studied particles (Stone et al. 2019). Another important finding is the H/He ratio of 12.6 ± 0.6 measured by Voyager 1 at low energies (Stone et al. 2013). The Galactic H/He ratio is energy dependent, ranging from values as high as $\sim$16 at low energies to values as low as $\sim$4 at high energies (Abe et al. 2016). The values very often given for GCRs, i.e., 87% protons and 12% He, represent something like an average. The experimental results from both Voyager missions are the only and therefore the most important data characterizing the LIS in the low-energy regime, i.e., below $\sim$1 GeV.

Characterizing the LIS at higher energies is much easier because highly energetic particles in the energy range of $\sim$2 TeV or higher are largely unaffected by solar modulation and so the spectra measured by BESS, PAMELA, AMS-01, and AMS-02 near Earth are excellent proxies for the LIS.

Several LIS parameterizations exist in the literature and fall into two categories: the approaches before the Voyager missions left the heliosphere and the ones developed after these events. Here we briefly summarize some of the approaches often used, starting with the parameterizations developed before the LIS Voyager data. We focus on the data for LIS protons.

2.1.1. Pre-Voyager Models: Parameterization by Garcia-Munoz et al. (1975)

This spectrum is the base for the GCR model by Castagnoli & Lal (1980), which is very often used for studies of cosmogenic nuclides in meteorites, the lunar surface, terrestrial surface samples, and the production of ^{10}Be in the terrestrial atmosphere (e.g., Masarik & Beer 1999; Vonmoos et al. 2006; Ammon et al. 2008; Steinhilber et al. 2008; Leya & Masarik 2009). The parameterization is

$$J_{\text{LIS,GM75}}(E) = 9.9 \cdot 10^8 \times [E + 780 \times e^{-2.5 \cdot 10^{-4} \times E}]^{-2.65}. \tag{1}$$

J_{LIS} is in units of particles$/(\text{m}^2\,\text{s}\,\text{sr}\,(\text{MeV}/\text{nucleon}))$ and E is given in MeV. In the following, we refer to this spectrum as GM75.

2.1.2. Pre-Voyager Models: Parameterization by Webber & Higbie (2003)

Another pre-Voyager approximation for the LIS proton spectrum was published by Webber & Higbie (2003), in the following labeled WH03

$$J_{\text{LIS,WH03}}(E) = \frac{2.11 \cdot 10^4 \times E^{-2.80}}{1 + 5.85 \cdot E^{-1.22} + 1.18 \cdot E^{-2.54}}, \tag{2}$$

where E and J_{LIS} are given in GeV and particles$/(\text{m}^2\,\text{s}\,\text{sr}\,\text{GeV})$, respectively. Because the parameterization is only for protons, the energy per nucleon is equal to the energy.

2.1.3. Pre-Voyager Models: Parameterization by Usoskin et al. (2005)

The approach published by Usoskin et al. (2005) is based on an earlier approach by Burger et al. (2000), which was originally developed to describe the GCR gradients measured by the Ulysses spacecraft. The parameterization is given by

$$J_{\text{LIS,US05}}(E) = \frac{1.9 \cdot 10^4 \times P(E)^{-2.78}}{1 + 0.4866 \cdot P(E)^{-2.51}}, \tag{3}$$

with the rigidity calculated via $P(E) = \sqrt{E(E + 2E_r)}$ and $E_r = 938\,\text{MeV}$ the rest mass of the proton. J_{LIS} and E are expressed in units particles$/(\text{m}^2\,\text{sr}\,\text{s}\,(\text{GeV}\,\text{nucleon}^{-1}))$ and $\text{GeV}\,\text{nucleon}^{-1}$, respectively. For the following discussion, we refer to this spectrum as US05.

2.1.4. Pre-Voyager Models: Parameterization by Langner et al. (2003)

The LIS parameterization given by Langner et al. (2003) is based on a rather complex model describing the propagation of different particles in the Galaxy (Moskalenko et al. 2002). The LIS for protons—labeled LA03 in the following—given in the units particles$/(\text{m}^2\,\text{s}\,\text{sr}\,(\text{MeV}\,\text{nucleon}^{-1}))$ is calculated via

$$J_{\text{LIS,LA03}}(E) = \exp(0.823 - 0.08 \times (\ln(E))^2 + 1.105$$
$$\times \ln(E) - 9.202 \cdot 10^{-2} \times \sqrt{E}): \text{for } E < 1\,\text{GeV}\,\text{nucleon}^{-1}$$
$$= \exp\left(22.976 - 2.86 \times \ln(E) - \frac{1.5 \cdot 10^3}{E}\right)$$
$$:\text{for } E \geqslant 1\,\text{GeV}\,\text{nucleon}^{-1}. \tag{4}$$

2.1.5. Pre-Voyager Models: Parameterization by Webber & Higbie (2009)

Webber & Higbie (2009) used a Monte Carlo diffusion model to calculate the LIS for protons and helium, carbon, and iron nuclei. While they give the results only in tabular form, Herbst et al. (2010) developed the following parameterization for protons:

$$J_{\text{LIS,WH09}}(E) = \exp(-124.48 - 51.84 \cdot \ln[(\ln(E))]^2$$
$$+ 131.65 \cdot \sqrt{\ln(E)} - 241.73 \cdot (\ln(E))^{-1}$$
$$+ 376.66 \cdot (\ln(E))^{-2})$$
$$:\text{for } E < 1\,\text{GeV}\,\text{nucleon}^{-1}$$
$$= \exp(-51.69 \cdot \ln[(\ln(E))]^2 + 103.59 \cdot \sqrt{\ln(E)}$$
$$- 709.71 \cdot (\ln(E))^{-1} + 1161.56 \cdot (\ln(E))^{-2})$$
$$:\text{for } E \geqslant 1\,\text{GeV}\,\text{nucleon}^{-1}. \tag{5}$$

The thus calculated LIS—in the following labeled WH09—has the units particles$/(\text{m}^2\,\text{s}\,\text{sr}\,(\text{MeV}\,\text{nucleon}^{-1}))$.

2.1.6. Post-Voyager Models: Parameterization by Della Torre et al. (2016) and Boshini et al. (2020)

The approach by Della Torre et al. (2016) combines two transport models, one describing particle transport in the interstellar space and one for the particle transport in the heliosphere. The model combination is used to reproduce the experimental cosmic-ray particle fluxes at different levels of solar modulation and at both polarities of the solar magnetic field using the LIS as a variable to start with. The thus-deduced LIS is in accord with both the low-energy Voyager measurements and the high-energy data from BESS, PAMELA, AMS-01, and AMS-02. The parameterization is

$$J_{\text{LIS,DT16}}(E) = [94.1 - 831 \cdot P(E) + 16700 \cdot P(E)^3$$
$$- 10200 \cdot P(E)^5] \times P(E)^{-2.7} \text{ (for } P(E) \leqslant 1\,\text{GV})$$
$$= 10800 + \left[\frac{8590}{P(E)} - \frac{4230000}{3190 + P(E)} + \frac{274000}{17.4 + P(E)}\right.$$
$$\left. - \frac{39400}{0.464 + P(E)}\right] \times P(E)^{-2.7} \text{ (for } P(E) > 1\,\text{GV}). \tag{6}$$

The flux is in units of particles$/(\text{m}^2\,\text{s}\,\text{sr}\,\text{GV})$ and $P(E)$ is the rigidity in GV calculated as shown in Section 2.1.3. In the following, we refer to this spectrum as DT16. Note that the same set of equations is also given by Boshini et al. (2018). In a follow-up study and by using the same model combination, one model for interstellar and one model for heliospheric transport, Boshini et al. (2020) adjusted the parameterization with the goal to describe the LIS for all cosmic-ray particles with $Z \leqslant 28$. In their publication, the results are only given in tabular form. For the following discussion, we refer to the proton LIS as BO20.

2.1.7. Post-Voyager Models: Parameterization by Vos & Potgieter (2015)

The LIS for protons proposed by Vos & Potgieter (2015)—in the following labeled VP15—can be calculated via

$$J_{\text{LIS,VP15}}(E) = 2.7 \cdot 10^3 \times \frac{E^{1.12}}{\beta^2} \times \left(\frac{E + 0.67}{1.67}\right)^{-3.93}, \tag{7}$$
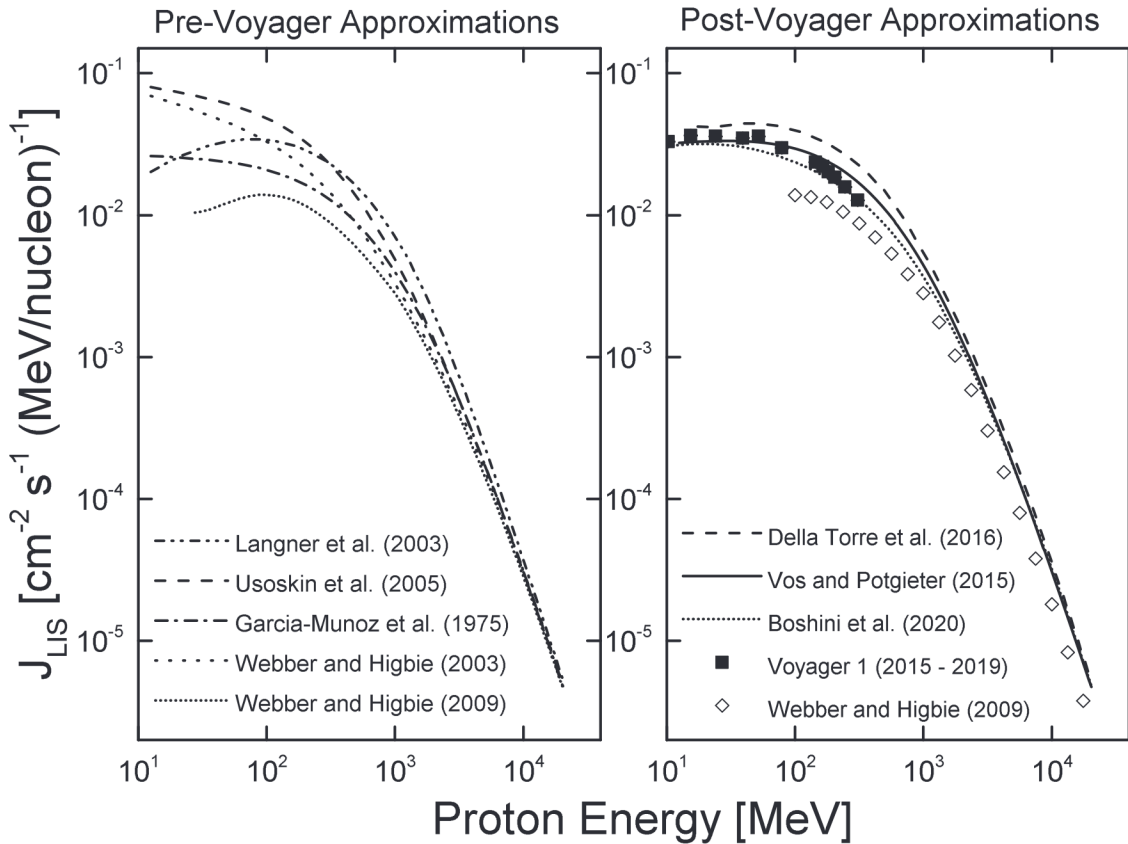
Figure 1. Differential local interstellar proton spectra in particles/(m² s sr MeV) as a function of proton energy in (MeV). The parameterizations developed before Voyager data from outside the heliosphere were available are shown in the left panel. The right panel shows more recent approaches developed by considering the interstellar Voyager data. In addition, data from Voyager 1 from 2015 to 2019 are shown as black squares, and the LIS calculated by Webber & Higbie (2009) are shown as open diamonds.

with $\beta = v/c$ the ratio of the proton velocity relative to the speed of light and J_{LIS} and E are given in particles/(m² s sr (GeV nucleon^{-1})) and GeV, respectively. The same equation is given by Usoskin et al. (2017).

2.1.8. The Different LIS Spectra

Figure 1 depicts the LIS for Galactic protons. The left panel shows the parameterizations published before Voyager data from outside the heliosphere were available. It can be seen that the various approaches differ significantly, especially at low energies. At higher energies, i.e., >10 GeV, all parameterizations give similar flux densities J, which is of no surprise because for particles in this energy range, solar modulation effects are only very minor and the spectra measured in the inner solar system are good proxies for the LIS. At lower energies, modulation effects are important and the calculated LIS depends on the transport model used to calculate it. Such transport models are parameter dependent, i.e., they depend, among other things, on the choice of the diffusion constant and the size and position of the heliosheet. Consequently, the calculated LIS at low energies also depends on the choice of such parameters. In this low-energy range, the different approaches vary significantly. For example, the LIS given by Usoskin et al. (2005) at a few tens of MeV is almost one order of magnitude higher than the LIS given by Webber & Higbie (2009) in the same energy range. Interestingly, the different approaches can be categorized into those showing high flux densities at low energies with continuously decreasing flux densities toward higher energies (Garcia-Munoz et al. 1975; Webber & Higbie 2003; Usoskin et al. 2005) and those showing a local maximum in the range of ~100 MeV (Langner et al. 2003; Webber & Higbie 2009).

The more recent approaches developed using the interstellar Voyager data are shown in the right panel of Figure 1. We also show the fluxes provided by Voyager 1 from 2015 to 2019, i.e., after Voyager 1 left the heliosphere (black squares). The uncertainties, which are smaller than the symbol sizes, only comprise the statistical uncertainties given by the different Voyager instruments (http://voyager.gsfc.nasa.gov). Systematic uncertainties are not taken into account. Also shown is the LIS calculated by Webber & Higbie (2009, open diamonds). All three parameterizations, Bo20, VP15, and the result given by Webber & Higbie (2009), give very similar results, and all three approaches describe the low-energy data from Voyager 1 and 2 reasonably well.

Almost all models of cosmic-ray transport assume that the LIS particles enter the heliosphere isotropically. However, there have been arguments that this might not always be true (Ngobeni & Potgieter 2011, 2012).

2.2. Solar Modulation of Galactic Cosmic Rays

The major physical processes relevant for cosmic-ray modulation are diffusion caused by irregularities in the heliospheric magnetic field, convection and adiabatic energy loss in the outward-moving expanding solar wind, and gradient and curvature drifts caused by large-scale structures of the

heliospheric magnetic field. Therefore, the GCR spectrum inside the heliosphere is a function of position, energy, and time (for more information see, e.g., Fujii & McDonald 1997; Potgieter 2013). Solar modulation is especially important for particles with energies below ~ 30 GeV nucleon^{-1}, for which the fluxes can vary by about one order of magnitude (Potgieter 2013).

The dominant and most important timescale relevant for GCR modulation is the 11 yr solar cycle, which is related to the solar sunspot number. Very important is also the 22 yr solar cycle, which is caused by the reversal of the solar magnetic field during each period of extreme solar activity. Depending on the polarity of the solar magnetic field, GCR particles will reach the inner solar system from different heliospheric directions. During the $A < 0$ polarity cycle, protons (and other positively charged particles) drift inwards mainly through the equatorial region of the heliosphere. In contrast, during the $A > 0$ polarity cycles, positively charged particles drift inwards mainly over the poles. It is obvious that the vastly different particle trajectories will result in differences in the particle spectra and also in the intensity gradients (increasing fluxes with increasing heliocentric distance) between the two solar polarity cycles (see also Section 2.3). Additionally, there are short periodic modulation changes of 25–27 days caused by the solar rotation, and finally, there are indications of GCR intensity cycles of 50–65, 90–130, 200, and 600 yr. However, it is not clear whether these are real periodic variations or perturbations. For a recent review on the solar modulation of cosmic rays, see Potgieter (2013).

When studying solar modulation effects in the forced-field approximation (see below), the modulation effect can be parameterized using the particle-dependent solar modulation parameter ϕ_i. Because particles with the same rigidities have the same trajectories, the approach can be generalized by using the (particle-independent) solar modulation function Φ, which is related to the solar modulation parameter ϕ_i via

$$\Phi = \phi \times \frac{e Z_i}{A_i}, \qquad (8)$$

where Z_i and A_i are the charge and mass numbers of the nucleus of type i. The parameters ϕ and Φ are in units of MV and MeV, respectively. For single charged particles, i.e., protons, ϕ and Φ are the same. The solar modulation function is usually interpreted as the mean adiabatic energy loss. For example, a solar modulation $\Phi = 600$ MeV indicates that a (single charged) particle entering the solar system from outside the heliosphere suffers an adiabatic energy loss of 600 MeV per nucleon before reaching this location inside the heliosphere (Φ is a function of the heliocentric distance; see Section 4.4). Particles entering the solar system with lower energies would be screened out by the solar magnetic field. While this picture is very illustrative, the modulation function has no real physical meaning (Caballero-Lopez & Moraal 2004; Usoskin et al. 2017). However, for practical applications, the solar modulation function Φ is a very useful parameter describing solar modulation and with it the actual shape of the GCR particle spectrum in the inner solar system. Therefore, Φ is often used in practical applications, e.g., studying atmospheric ionization, climate modeling, and cosmogenic nuclide studies (see, e.g., Usoskin et al. 2017). According to Equation (8), for the same

solar modulation function, Galactic protons and Galactic α particles do not have the same energy loss.

Most modulation models are based on the numerical solution of the cosmic-ray transport equation originally developed by Parker (1965). In the simplified version, which is called the forced-field approximation and which is obtained by assuming azimuthal and spherical symmetry, the energy spectrum of the ith GCR species in the inner solar system is related to the unmodulated LIS of the same species via the solar modulation function Φ as

$$J_{\mathrm{GCR},i}(E, t) = J_{\mathrm{LIS},i}(E + \Phi(t))$$
$$\times \frac{E(E + m_p c^2)}{(E + \Phi(t))(E + \Phi(t) + 2 m_p c^2)}, \qquad (9)$$

with E the kinetic energy per nucleon. The only temporal variability is in the solar modulation function $\Phi = \Phi(t)$. For the LIS, any spectrum given in Section 2.1 can be used. For example, the recent study by Argento et al. (2015a, 2015b) used the following parameterization for calculating the differential proton fluxes in Earth's atmosphere and in terrestrial surface samples:

$$J_{\mathrm{GCR,US05}}(E, t) = J_{\mathrm{LIS,US05}}(E + \Phi(t))$$
$$\times \frac{E(E + m_p c^2)}{(E + \Phi(t))(E + \Phi(t) + 2 m_p c^2)}, \qquad (10)$$

with the kinetic energy E given in units of MeV, m_p the rest mass of the proton, and LIS the local interstellar spectrum given in Equation (3). The spectrum $J_{\mathrm{GCR,US05}}$ is given in the same units as the LIS, which usually is particles/(m^2 sr s (GeV nucleon^{-1})).

An approach very often used for cosmogenic nuclide studies in meteorites, the atmosphere, and terrestrial surface samples is the parameterization given by Castagnoli & Lal (1980):

$$J_{\mathrm{GCR,CL80}}(E, t)$$
$$= c_p \times \frac{E(E + 2 m_p c^2) \cdot (E + x + \Phi(t))^{-2.65}}{(E + \Phi(t))(E + 2 m_p c^2 + \Phi(t))}, \qquad (11)$$

with E the kinetic energy in MeV, Φ the solar modulation function in MV, and m_p the rest mass of the proton. The factor x is given by (in MeV):

$$x = 780 \times e^{-2.5 \cdot 10^{-4} \times E}. \qquad (12)$$

With the normalization factor $c_p = 9.9 \times 10^8$, the flux is given in units of particles/(m^2 s sr MeV). Because the parameterization is for protons, $\Phi = \phi$ and MeV nucleon^{-1} = MeV. This parameterization was first developed by Castagnoli & Lal (1980) and was later corrected by Masarik & Reedy (1996). Note that Equation (12) is not strictly correct because in the framework of the used forced-field approximation, the energy E has to be replaced by $E + \Phi(t)$ (see Equation (9)). In Equation (12), however, the E has not been replaced by $E + \Phi(t)$. In the forced-field approximation, Equation (12) should be written as

$$x = 780 \times e^{-2.5 \cdot 10^{-4} \times (E + \Phi(t))}. \qquad (13)$$

However, most cosmogenic nuclide studies on meteorites (e.g., McKinney et al. 2006; Ammon et al. 2008; Leya & Masarik 2009; Kim et al. 2010), the terrestrial atmosphere (e.g., Masarik & Beer 1999), and terrestrial surface samples are based on the GCR parameterization given in Equations (11) and (12).
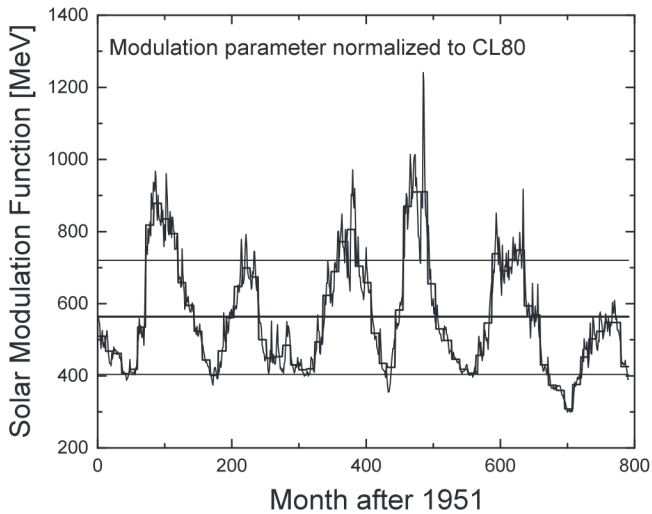
Figure 2. Solar modulation function normalized to the GCR spectrum given by Castagnoli & Lal ([1980](#)) as a function of time since 1951. The thin black line depicts the monthly values, and the thick black line shows the yearly averages. The effect of the 11 yr solar cycle is clearly visible. The average solar modulation potential is $\Phi = 564$ MeV (thick horizontal line) with a 1σ standard deviation of 158 MeV (thin horizontal lines)

In all approaches, the solar modulation function Φ is a model-dependent parameter because Φ depends on the choice of the LIS. It has been shown by Usoskin et al. ([2005](#)) and Herbst et al. ([2010](#)) that the same inner solar system GCR spectrum can be obtained via different LIS if the solar modulation function is chosen respectively. To be more quantitative and focusing on the spectra used in the following, we can use the finding by Usoskin et al. ([2005](#)) that there is an (almost) linear relationship between the different sets of modulation functions. The one relevant for us is

$$\Phi_{\mathrm{CL80}} = 0.97 \cdot \Phi_{\mathrm{US05}} - 78 \text{ MeV}. \qquad (14)$$

Consequently, a modulation function of $\Phi = 600$ MeV based on the CL80 model (Equation ([11](#))) we use as the long-term average for the meteoroid orbits (see below) corresponds to a modulation function of $\Phi \sim 700$ MeV if the spectrum given by Usoskin et al. ([2005](#)) is used (Equation ([10](#))). To emphasize, the GCR particle spectrum in the inner solar system can reliably be described using different combinations of LIS and solar modulation functions; see also Herbst et al. ([2010](#)). However, the need to use different values for the solar modulation for different LIS clearly demonstrates the importance to always relate the Φ value to the corresponding LIS used. For modeling cosmogenic nuclide production in meteorites, the Moon, the terrestrial atmosphere, and terrestrial surface samples, it is therefore not so important on which LIS parameterization the model is based as long as it is combined with the corresponding solar modulation function.

The new model calculations for cosmogenic nuclides rely on the GCR particle spectrum for protons given by Castagnoli & Lal ([1980](#)) and corrected by Masarik & Reedy ([1996](#)), and the approach we developed for Galactic α particles (see Section [3](#)). It is therefore important to emphasize that the long-term average solar modulation function for the meteoroid orbits, i.e., at ~3 au and at an orbital distance of 1 au (lunar samples) determined further below, is only valid for the Castagnoli–Lal spectrum.

In Figure [2](#), we show the monthly reconstructed solar modulation function given by Usoskin et al. ([2017](#)) renormalized to the solar modulation function corresponding to the

spectrum given by Castagnoli & Lal ([1980](#)). For the renormalization, we used Equation ([14](#)). After this adjustment, the monthly averaged modulation function can directly be compared to our results for the long-term averages in the inner solar system (see below). Note that this data is for a heliocentric distance of 1 au, i.e., it is for the orbit of Earth. For a discussion of the radial GCR intensity gradient, see Section [2.3](#).

Heliospheric modulation is not yet understood in detail, and there is no simple model capable of accurately describing the whole range of available data. This is mainly due to the increased precision of the experimental data, but it is also due to the improved reliability of the calculations for interstellar and heliospheric propagation (Moskalenko et al. [2002](#)).

2.3. Galactic Cosmic-Ray Radial Intensity Gradients

When discussing GCR intensity gradients, one has to distinguish between radial gradients, i.e., changes of the GCR flux with distance from the Sun, and gradients in heliospheric latitude, i.e., gradients when leaving the ecliptic. Here we focus on radial gradients because the orbits of most planetary bodies are in or at least close to the ecliptic. In general, there is a positive radial gradient from the inner solar system toward the outer solar system, i.e., the GCR intensity increases with distance from the Sun.

Early theoretical studies of GCR intensity gradients proposed that during solar magnetic field configurations in which positively charged particles drift into the inner solar system mostly via the solar poles ($A > 0$), the radial gradient should be much smaller than during the $A < 0$ periods, when the positively charged particles are drifting into the inner solar system mostly through the equatorial region (see also Section [2.2](#)). In addition, at solar maximum, the radial gradients are larger than at solar minimum (see, e.g., Fujii & McDonald [1997](#); Potgieter [2013](#)). Consequently, when discussing GCR intensity gradients, one always must give the extra information whether the value is for solar minimum or maximum conditions and for the $A > 0$ or $A < 0$ polarity cycles. For most of our studies, however, we need the long-term average GCR spectrum in the inner solar system and with it the GCR intensity gradient averaged over many 11 and 22 yr solar cycles. Exceptions are studies using short-lived nuclides, e.g., ^{22}Na, which very often are performed to study GCR variations. In the following, we give a short summary of our literature study.

By summarizing the results from the Pioneer 8–11 missions, McKibben ([1975](#)) concluded that there is a small radial gradient of a few percent per astronomical unit for particles $\geqslant 50$ MeV. Using data from Pioneer 10 and 11 up to 35 and 18 au, respectively, Walker et al. ([1985](#)) determined an average gradient of 2% au^{-1} with some superimposed time and energy dependencies.

Using data from Pioneer 10/11, Voyager 2, and IMP 6, 7, and 8 in the time window 1972–1996, Fujii & McDonald ([1997](#)) found large differences in the radial dependency between solar minimum and solar maximum conditions. They determined radial gradients at 1 au of ~13% au^{-1} and ~5.5% au^{-1} for the solar minima 1977 and 1987, respectively. For the same solar minima but at 5 au, the radial gradient was ~4% au^{-1}. The data therefore indicate that at solar minimum conditions, the GCR intensity gradient decreases with increasing distance from the Sun. At the solar maxima 1981 and 1990, the radial gradients at 1 au were ~1% au^{-1} and at 5 au they

were $\sim$2% au^{-1}, i.e., the radial gradient increased with increasing heliocentric distance. Note that the results were derived from proton data in the energy interval 130–220 MeV; they are therefore not representative for the entire GCR spectrum. It has already been pointed out by Fujii & McDonald (1997) that the radial gradients of the integral number of ions >70 MeV are likely less sensitive to spatial and temporal changes of the modulation conditions. Surprisingly, the results by Fujii & McDonald (1997) give a higher GCR intensity gradient (at least in the inner solar system) during solar minima than during solar maxima, opposite to what is theoretically expected and also opposite to their own conclusions.

With a data set similar to the one considered by Fujii & McDonald (1997), McDonald et al. (2003) studied the radial distribution of cosmic rays in the heliosphere at solar maximum conditions. Using data for the solar maxima of cycles 21, 22, and 23, they found a radial gradient of $\sim$10%/r au^{-1}, with r the radial distance in astronomical units. They found that the gradient is relatively constant in the inner heliosphere. This gave a radial intensity gradient of $\sim$10% au^{-1} at 1 au and $\sim$2% au^{-1} at 5 au. Therefore, in contrast to the earlier study, the data indicate that the radial gradient decreases with increasing heliocentric distance at solar maximum conditions. After a transition region in the range $\sim$10 and $\sim$20 au, the gradient increases to a much larger value of $\sim$73%/r au^{-1} that is almost constant between $\sim$25 and $\sim$82 au.

Using data from the HELIOS experiment 6, Marquard & Heber (2019) determined mean values for the solar modulation function for protons of 474 ± 28 MeV and 435 ± 23 MeV for the time intervals 1974 to the end of 1978 and from 1974 December to the end of 1977, respectively. In addition, they found a radial gradient for GCR particles with energies above 50 MeV nucleon^{-1} and up to a few hundred MeV nucleon^{-1} and in the range 0.3–1 au of $6.6 \pm 4\%$ au^{-1}.

Studying data from Ulysses and ACE in the energy range 125–200 MeV nucleon^{-1} for helium and 147–198 MeV nucleon^{-1} for carbon in the time period from 1997 to 2006, Gieseler et al. (2008) found a radial intensity gradient of $4.5 \pm 0.6\%$ au^{-1}. The studied time period covers the solar minima in the $A > 0$ periodic cycle, the polarity reversal to an $A < 0$ polarity cycle at the solar maximum, and the declining phase of solar cycle 23. The authors claim that this period is well suited to determine the mean radial gradient.

During the extended minimum of solar cycle 23 and by studying protons in the rigidity interval 1.6–1.8 GV, De Simone et al. (2011) determined a radial gradient of 2.7% au^{-1}.

Considering the finding that GCR intensity gradients significantly differ for solar maxima and minima conditions, the data obtained by Morales-Olivares & Caballero-López (2009) of $\sim$8% au^{-1} at 1 au and $\sim$16% au^{-1} at 5 au for protons in the energy range 130–220 MeV and at solar maximum conditions are only of limited relevance for the study of long-term average GCR intensity gradients needed for cosmogenic nuclide studies. The same is true for the intensity gradients in the outer heliosphere during solar minimum conditions given by Florinski et al. (2013). These authors give values of $\sim$1% au^{-1} for 180 MeV protons, which is slightly lower than typical model gradients (1.5%–1.8% au^{-1}).

The discussion demonstrates that the GCR intensity gradient depends on solar activity (maximum, minimum), on the solar polarity cycles ($A < 0$, $A > 0$), and on the radial distance from the Sun. Considering now that the orbital distances for most meteorites are often not known and that the spacecraft data must be extrapolated backward in the past, it is obvious that none of the data can directly be applied to the long-term average needed for cosmogenic nuclide studies in meteorites, lunar surface samples, and Earth. Another approach has been introduced by Alexeev et al. (2019). These authors determined average GCR intensity gradients in the heliosphere by analyzing cosmogenic radionuclides in meteorites with known orbits and found—based on ^{26}Al activity concentrations—a long-term average of $26 \pm 18\%$ au^{-1} in the range 2–4.5 au, which is higher than most of the direct measurements.

Considering that the radial GCR intensity gradient is due to stronger solar modulation in the inner solar system than in the outer solar system, the solar modulation function for meteoroids in the asteroid belt at $\sim$3 au must be lower than the solar modulation function for Earth and Moon at 1 au. This is in striking contrast to the study by Argento et al. (2015a). These authors used the same modulation function $\Phi = 550$ MeV for the meteorite Knyahinya and for terrestrial surface samples, which cannot be correct. In addition, the study by Kim et al. (2010) also used the same modulation function for meteorites and lunar samples. However, they needed different values for the integral number of GCR particles, which is the spectra integrated over the energy and which has units of $1\,\mathrm{cm}^{-2}\,\mathrm{s}$, to describe the different cosmogenic nuclides in the meteorite Knyahinya and the Apollo 15 drill core. In their study, the integral number for ^{10}Be is 13% higher for the meteorite Knyahinya than for the Moon. For ^{26}Al the integral number of GCR particles for meteorites is 26% higher than for the Moon. For both nuclides, ^{10}Be and ^{26}Al, they needed a higher number of GCR particles for the meteorite Knyahinya than for the Moon, in agreement with an expected positive radial gradient. Note that a higher integral number of GCR particles corresponds to a lower solar modulation function. On the contrary, for ^{14}C they needed an integral number of GCR particles $\sim$26% higher for the Moon than for meteorites, opposite to what is expected and to their results for ^{10}Be and ^{26}Al.

A consistent and reliable model for the production of cosmogenic nuclides in inner solar system objects must be able to describe all cosmogenic nuclides (stable or with a similar half-life) in meteorites with the same solar modulation function because most meteorites share similar orbital distances. Furthermore, the solar modulation function for Moon and Earth must be slightly higher than the solar modulation function for the meteorite orbits; the differences are given by the radial gradient of the GCR intensity. The solar modulation functions we deduced for the meteorite orbits and the Moon are discussed in Sections 4.1 and 4.3.

2.4. Long-term Temporal Variation of the Galactic Cosmic Rays

In addition to the radial GCR intensity gradient just discussed (Section 2.3) and in addition to the short-term modulation effects caused by temporal changes of the modulation processes within the heliosphere (see Section 2.2), which average out when discussing long-lived (half-lives in the range of a few hundred thousand to a few million years) or stable cosmogenic nuclides, there is the possibility for long periodic changes in the GCR intensity caused by variations in the LIS. Variations in the LIS can have the following causes: first, and probably most

importantly, variations from spiral arm passages, which occur over timescales of $\sim 10^8$ yr. The typical lifetimes of massive stars that at their end produce supernovae, and therefore produce not only the ingredients for GCRs but also the setting needed for particle acceleration, are relatively short. Consequently, stars and supernova form at very similar locations, and hence places with a higher star formation rate (SFR) are also the places for higher supernova rates and higher GCR intensities. Because SFRs are higher in Galactic spiral arms than in interarm regions, it is expected that GCR intensities are also higher in Galactic spiral arms than in interarm regions. The Sun crosses Galactic spiral arms every ~ 150 Myr, which can result in periodic GCR intensity changes (Forman & Schaeffer 1979; Shaviv 2002, 2003). Shaviv (2002, 2003) calculated that the LIS fluences inside Galactic spiral arms might be up to a factor of 3 higher than in the interarm regions. Using the same model, Scherer et al. (2006) calculated that LIS fluence variations between the spiral arm and interarm regions can be in the range of 25%–135% of the current value, i.e., the variation can be almost a factor of 4. Sloan & Wolfendale (2013) questioned these numbers. According to their calculations, LIS intensity variations between the spiral arm and interarm regions can only be in the range 10%–20% and not more than $\sim 30\%$. Second, the SFR in the Milky Way might vary over long timescales, i.e., over timescales in the range of Gyr (see, e.g., Scherer et al. 2006). Third, local inhomogeneities in the Galactic environment might influence the inner solar system GCR spectrum. Here the argument is as follows. Changes in the geometrical structure of the heliosphere can affect the modulation of GCRs in the solar system. The geometrical configuration and the position of the heliopause change if the heliosphere moves in and out of denser regions in the ISM. Models indicate that the differences are most significant for relatively low-energy particles and at radial distances larger than ~ 60 au. Compression of the heliosphere results in an increase of the GCR fluence in the inner solar system. For more information, see, e.g., Vahia (2004, 2006). Fourth, the occurrence of nearby supernovae can have profound but very local and likely short-lived effects on the local LIS intensities.

3. Model Calculations

The basics of the model calculations for cosmogenic nuclide production rates are the same as what we used earlier (Ammon et al. 2008; Leya & Masarik 2009), i.e., the model is based on the spectra of primary and secondary particles calculated using Monte Carlo methods and on the energy-dependent cross sections for the relevant nuclear reactions (see also Section 3.5). However, this new version of model calculations (labeled version V03) differs in some very important points from our earlier approaches. First, the particle spectra are no longer calculated using the LAHET code system but by using the Geant4 toolkit (see Section 3.1). Second, this is the first version of model calculations able to include primary and secondary Galactic α particles (see Section 3.2). Third, there was a need to restudy and adjust some of the relevant cross sections due to a change in the accepted half-life (e.g., ^{10}Be) and/or due to a change in standards used for accelerator mass spectrometry (AMS, e.g., ^{10}Be and ^{26}Al; see Section 3.3). Here we briefly discuss some of the changes and improvements.

3.1. CosmicTansmutation, Geant4, and INCL++6

The Monte Carlo toolkit Geant4 (GEometry ANd Tracking) is a transport model originally designed for high-energy interactions (Agostinelli et al. 2003). However, Geant4 provides a comprehensive set of models covering all physical processes important for nuclear interactions and transport over a wide energy range, i.e., from a few meV for neutrons up to TeV for all particles. In addition, Geant4 is a well-developed open source program and allows the user to define the geometry, the particle sources, and other relevant physical aspects in a very flexible way. To benefit from this, we developed a new computer code called CosmicTransmutation, which is designed to produce all of the relevant input information for Geant4 and to help the user to extract the results from the sometimes very large output files (Hirtz 2019). Thanks to the CosmicTransmutation interface, we are able to routinely and reliably calculate the particle spectra for meteoroids (spherical and elliptical) and for planetary surfaces and planetary atmospheres (including magnetic fields). Here we focus on spherical meteoroids and the lunar surface.

In Geant4, the user chooses from a large list of available physics modules. In CosmicTransmutation, the default physics list is "FTFP_INCLXX_HP." In this physics list, the Fritiof model (FTF) in combination with the precompound model "Preco" is used for high energies, i.e., for energies above 15 GeV for hadrons and above 2.9 GeV nucleon^{-1} for ions (Ushinsky 2010). At intermediate energies, INCL is used for the intranuclear cascade, i.e., for this part of a nuclear reaction that can be described via individual particle-particle collisions (Serber 1947). The definition of what is an intermediate energy in INCL depends on the particle type. In the latest version of Geant4.10.05, INCL treats nucleons, i.e., protons and neutrons, between 1 MeV and 20 GeV. For heavy ions, and notably for α particles, INCL is used between 0 and 3 GeV nucleon^{-1}. However, in the physics list FTFP_INCLXX_HP we used, the INCL code treats neutrons only down to 20 MeV. At lower energies, we rely on the "High Precision Neutron Model," which is based on tabulated values from various data compilations for neutrons down to 10^{-12} eV. The physics list chosen provides a sufficient overlap of the individual models in the different energy ranges for smoothing.

The current version of INCL is able to reliably handle α-induced reactions and is also able to properly treat the emission of light charged ejectiles up to mass number $A = 8$ (Mancusi et al. 2014). In addition, we recently added strange particles to the INCL code, which extends the applicability of the code up to an energy of ~ 20 GeV. This is probably not that relevant for modeling cosmogenic nuclides in meteorites and the lunar surface but it is important for modeling nuclide production in Earth's atmosphere or on Earth's surface where the cutoff caused by Earth's magnetic field is important. For more information about the current INCL version, called INCL++6, see, e.g., Hirtz et al. (2018, 2020) and David & Leya (2019).

The recent study by Li et al. (2017) modeling cosmogenic nuclides on the Moon is also based on the Geant4 simulation toolkit but did not use the latest version of the INCL++6 code, which was not available at that time. Instead, they used the "Binary Cascade" approach for modeling the intranuclear cascade, which is different from the INCL code we used. Also, the study by Dong et al. (2014) used the Geant4 software package to study cosmogenic nuclide production rates on the

lunar surface. However, they give no further details on the chosen underlying physical models that they used.

The Geant4 calculations were performed on a dedicated desktop computer having four processors enabling the calculation of four threads in parallel. In this setup, calculating the trajectories of 2 million particles in an L-chondrite with a radius of 45 cm takes ~1 day and the calculation for the Moon takes ~5 days.

3.2. Particle Sources

One of the most important input data for any model of cosmogenic nuclides is the GCR particle spectrum. For a

which is based on the assumption that the spectrum for primary Galactic α particles is very similar to the spectrum for primary Galactic protons if both are discussed in terms of energy per nucleon (87% protons and 12% α's). The parameterization we developed is only based on the solar modulation function for protons Φ. By choosing Φ, we can calculate a new parameter k via

$$k = (1.786 \cdot 10^{-3} \times \Phi) - 0.1323, \tag{15}$$

and from this, we can calculate the spectrum for Galactic α via

$$J_\alpha(E, k) = \frac{c_\alpha \times E^k \times (E + 2m_\alpha c^2)}{(E + 700) \times (E + 2m_\alpha c^2 + 700) \times (E + 312500 \cdot E^{-2.5} + 700)^{1.65+k}}, \tag{16}$$

careful discussion of the different LIS and the heliospheric modulation process, see Sections 2.1 and 2.2, respectively. As mentioned before, it is important to consider primary Galactic α particles (effectively including all heavier species) separately from primary Galactic protons because they are modulated differently, and they contribute 30%–50% of the total energy.

For primary Galactic protons, we use the spectrum originally developed by Castagnoli & Lal (1980), which was later corrected by Masarik & Reedy (1996; see also Equation (11)). As already mentioned above, this is the first version of model calculations that directly considers primary and secondary Galactic α particles. All earlier models for cosmogenic production rates in meteorites used the so-called α approximation (e.g., Ammon et al. 2008; Leya & Masarik 2009; Kim et al. 2010). Specifically, it has been assumed that every incoming primary Galactic α particle breaks up into four nucleons in the first inelastic collision. Further, it has been assumed that the α-particle-derived nucleons, e.g., two protons and two neutrons, each contains ~25% of the original α energy, i.e., that the total energy is approximately equally distributed among the nucleons. Next, it is assumed that the energy distribution of the four nucleons is similar to that of the primary Galactic protons. Ignoring differences in the production of secondary particles between proton- and neutron-induced reactions and considering that GCRs consist of ~87% protons and ~12% α particles, the contribution from primary GCR α particles to the total production rates were approximated by multiplying the production rates obtained for protons and neutrons by a factor of 1.55. It was always obvious that this approximation cannot be valid for the production of cosmogenic ^{4}He (an important cosmogenic nuclide for iron meteorite studies), and it is also expected that the approximation fails for certain low-energy reactions. This is because every α particle reacting directly and not breaking up into four nucleons produces cosmogenic nuclides but the number of secondary particles produced in this reaction is expected to be much smaller than the number of secondary particles assumed to be produced by two protons and two neutrons, i.e., after the α breakup. Consequently, every α particle reacting directly reduces the (assumed) secondary particle fluxes and therefore reduces the production rates.

For the code CosmicTransmutation, we developed a parameterized version of the primary Galactic α spectrum,

with E the kinetic energy in MeV nucleon^{-1} and $c_\alpha = 5.5 \times 10^7$ for a particle flux in units of particles/(m^2 s sr (MeV nucleon^{-1})).

We developed this parameterization of the primary Galactic α spectrum to make the model calculations more convenient. By doing so, we can calculate the particle spectra in meteorites, planetary atmospheres, and planetary surfaces simply by using only one value for the solar modulation function Φ. Equation (16) should only be considered as a convenient model input; it is not the result of heliospheric transport and modulation calculations.

3.3. Cross Sections

The cross-section database adopted is very similar to the one we used earlier (Ammon et al. 2008; Leya & Masarik 2009). Here we summarize the improvements and changes relevant for the three cosmogenic nuclides discussed here: ^{10}Be, ^{26}Al, and ^{22}Na. The ^{10}Be cross sections were recalculated for the new ^{10}Be half-life (Nishiizumi et al. 2007; Chmeleff et al. 2010), and some of the cross sections, those measured at ETH Zürich, needed to be renormalized to a change in the AMS standard (Christl et al. 2013). The change in the ^{10}Be half-life only affected the cross sections (and thick target data; see further below), not the ^{10}Be activity concentrations in meteorites and/or the lunar surface. In addition, we renormalized some of the ^{26}Al cross sections (and thick target data) due to the recent change of the ^{26}Al standard used at the ETH Zürich AMS facility. The excitation functions for the proton-induced reactions consist mostly of experimental data from the EXFOR database; missing data were calculated using results from INCL ++6. For some cases, we double-checked and extended the low-energy part of the excitation functions, especially the region close to the reaction threshold, using TALYS predictions (Koning & Rochman 2012). The same is true for α-induced reactions, although more inter- and extrapolations using INCL++6 and/or TALYS were necessary. For neutron-induced reactions, we recalculated a posteriori neutron excitation functions using our energy-dependent deconvolution procedure using renormalized ^{10}Be and ^{26}Al data and INCL++6 results as guess functions. For more information, see Leya & Michel (2011). For ^{22}Na, we are in a comfortable situation that high-energy neutron-induced cross sections exist for the

Table 1
Chemical Composition (weight%) and Density (g cm^{-3}) Used for the Model Calculations

Chemical Element	Apollo 15 (weight%)	Average L-chondrites (weight%)	Knyahinya (weight%)
C	⋯	0.09	0.34
O	42.43	37.44	37.67
Na	0.30	0.70	0.79
Mg	7.02	14.9	15.14
Al	5.79	1.22	1.34
Si	21.97	18.5	19.02
P	⋯	0.095	0.14
S	0.06	2.20	2.31
K	0.25	0.0825	0.11
Ca	6.15	1.31	1.12
Ti	1.11	0.063	0.06
Cr	⋯	0.388	0.45
Mn	⋯	0.257	0.23
Fe	14.72	21.5	20.15
Ni	⋯	1.20	1.04
ρ (g cm^{-3})	1.76	3.50	3.49

target elements Mg, Al, and Si, which are the most relevant target elements for cosmogenic ^{22}Na production in stony meteorites and the lunar surface (Michel et al. 2015). The excitation functions for the proton-, neutron, and α-induced production of ^{10}Be, ^{26}Al, and ^{22}Na can be found at https://doi.org/10.7910/DVN/IXZU6I.

3.4. Irradiated Material

The L-chondrite Knyahinya is modeled as a spherical body with a radius of 45 cm, which has been divided into 18 concentric shells, each with a thickness of 2.5 cm. For the Monte Carlo calculations, we use the average chemical composition for L-chondrites given in Table 1. The average chemical composition, which is only slightly different from the chemical composition for Knyahinya, is well applicable to the large variety of L-chondrites we plan studying. Note that the average composition is only used for calculating the differential particle spectra; the production rates for Knyahinya discussed below were calculated using its individual chemical composition also given in Table 1 (see also Mason & Wiik 1963).

The Moon is modeled as a spherical body with a radius of 1 km. We checked that the particle spectra calculated for objects with radii larger than or equal to 1 km are indistinguishable. For modeling the particle spectra for the Moon, we use the material and density of the Apollo 15 drill core. The composition (mass percent; Gold et al. 1977) is as follows: SiO$_2$ (46.4%), TiO$_2$ (1.82%), Al$_2$O$_3$ (10.8%), FeO (18.7%), MnO (0.12%), MgO (11.5%), CaO (8.58%), Na$_2$O (0.4%), and K$_2$O (0.3%). The chemical composition data (in weight %) are also given in Table 1. For the density of the Apollo 15 drill core, we use a value of $\rho = 1.76$ g cm^{-3} (Carrier 1974). For the Geant4 calculations, we divided the surface of the Moon into 100 layers, each 2.5 cm thick. The covered depth of 250 cm therefore corresponds to 440 g cm^{-2}. So far, we assume for the model calculations a homogeneous target composition. Because this is not always true and we expect especially the thermal and epithermal neutron fluxes to depend on the local chemical composition, studies including nonhomogeneous samples are planned.

3.5. Calculating Production Rates

Based on the particle spectra $J_m(E, R, d, \Phi)$ (particles/(cm^2 s MeV)), where ($m = 1$) for protons, ($m = 2$) for neutrons, and ($m = 3$) for α and the excitations functions for the production of nuclide j from the target element n by reactions induced by particle type m, $\sigma_{j,m,n}(E)$ (cm^2), we calculate the production rate $P_j(R, d, \Phi)$ (1/(g s)) for cosmogenic nuclide j via

$$P_j(R, d, \Phi) = \sum_{n=1}^{N} c_n \frac{N_A}{A_n} \sum_{m=1}^{3} \int_0^{\infty} \sigma_{j,m,n}(E)$$
$$\times J_m(E, R, d, \Phi) \times dE. \quad (17)$$

As discussed before, the differential particle spectra and with it the production rates depend on the radius R of the irradiated object, the depth d below the surface, and the solar modulation function Φ.

4. Results

Here we present the first results of the new model calculations, where we focus on ^{10}Be and ^{26}Al because high-quality data exist for Knyahinya (L-chondrite, reference for meteoroid orbits) and for the lunar surface (reference for 1 au). In addition, we calculate production rates for ^{22}Na to study short-term GCR variations. In this introduction study, we focus on Knyahinya, an L-chondrite with a radius of 45 cm, and the Apollo 15 drill core. Results for other cosmogenic nuclides, other meteorite types, and other radii will be presented in later publications. Production rates for ^{10}Be, ^{26}Al, and ^{22}Na in L-chondrites with radii between 4 and 500 cm can be found as Excel files at https://doi.org/10.7910/DVN/T5DOCN.

4.1. Results for the Knyahinya Meteorite—GCRs in the Meteoroid Orbit

Here we present the result of the new version of the model calculations. Using the CosmicTransmutation model, we calculated particle spectra for L-chondrites with a radius of 45 cm. The objects have been divided into 18 concentric shells, each with a thickness of 2.5 cm. Such an object is a very good description of the L-chondrite Knyahinya. This meteorite is well suited for such a study, because its preatmospheric shape and size have been carefully reconstructed (Graf et al. 1990a, 1990b). In addition, Knyahinya is an observed fall and has an exposure age of ∼40 Ma, providing that the irradiation took place in a single stage and that the radionuclides are in saturation.

To calculate the spectra for primary protons and α particles, secondary protons, secondary neutrons, and secondary α particles, we varied the solar modulation function from $\Phi = 100$ MeV to $\Phi = 1000$ MeV in steps of 50 MeV, i.e., we calculated 19 spectra. To obtain good statistics for the Monte Carlo calculations, we used 2 million incoming particles for each simulation. The calculated particle spectra can be found at https://doi.org/10.7910/DVN/SDVHT5. For each spectrum, i.e., for each modulation function, we calculated the depth profiles for ^{10}Be and ^{26}Al and compared the results to measured data (Graf et al. 1990b). We found a good agreement between measured and modeled depth profiles for a solar modulation function $\Phi = 600$ MeV. The ratios between modeled and measured production rates averaged over all shielding depths are for both nuclides close to 1.0. The standard
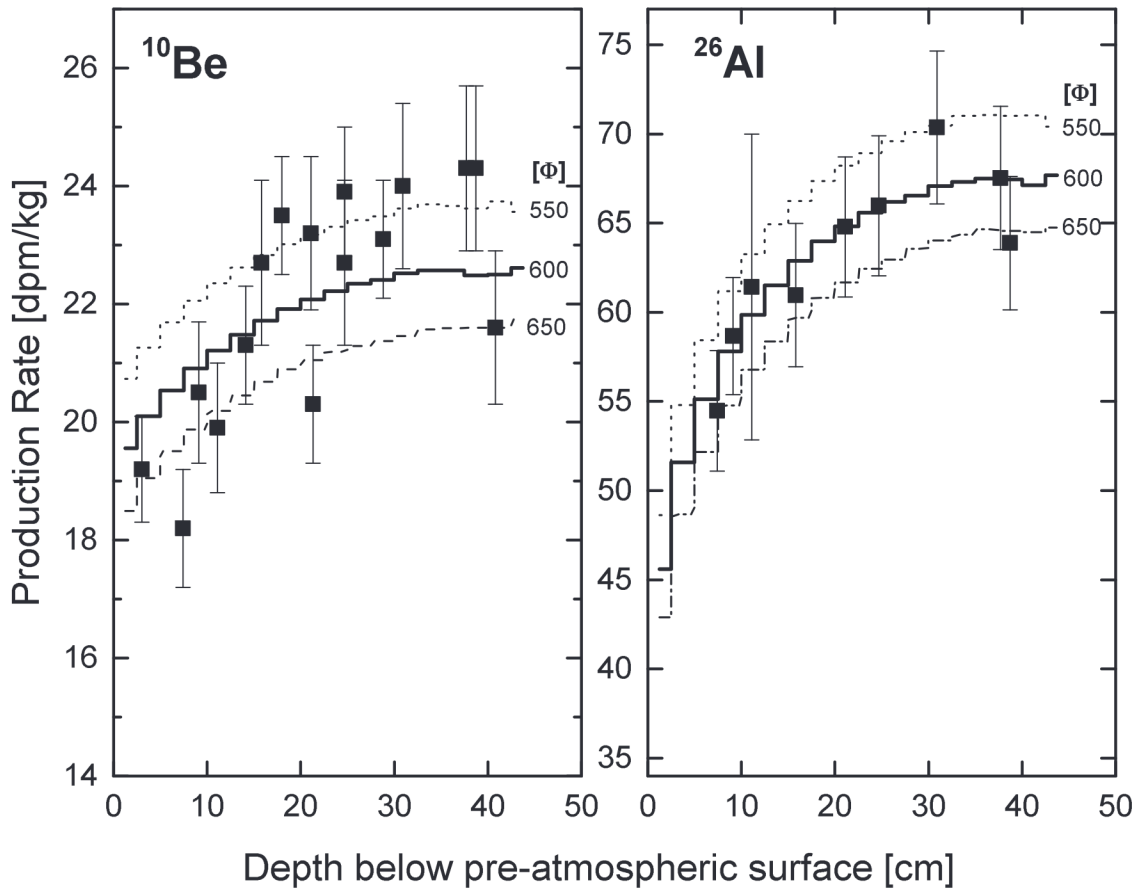
Figure 3. Depth profiles of ^{10}Be (left panel) and ^{26}Al (right panel) in the L-chondrite Knyahinya. The experimental data are from Graf et al. (1990b) renormalized to changed AMS standards. We show depth profiles for solar modulation functions $\Phi = 550$, 600, and 650 MeV. Both depth profiles can simultaneously be described using a solar modulation function $\Phi = 600$ MeV.

deviations for ^{10}Be and ^{26}Al are 0.06 and 0.03, which is close to the experimental uncertainties.

Figure 3 clearly demonstrates that model calculations using $\Phi = 550$ MeV or $\Phi = 650$ MeV give a worse description of the experimental data. From this, we can conclude that our result for the long-term average solar modulation function of $\Phi = 600$ MeV likely has an uncertainty of less than $\Delta\Phi = 50$ MeV. However, the result is model dependent, i.e., it depends significantly on the cross-section database used for modeling and on the choice for the LIS (see above). Because the cross sections we used are based on experimental data for proton-induced reactions, adjusted neutron cross sections, partly anchored to the few experimental data available, and on α-induced cross sections calculated using the very reliable INCL++6 code, we conclude that our result for the long-term average solar modulation function in the meteoroid orbit of $\Phi = 600$ MeV is relatively robust.

Our earlier model was able to simultaneously describe the ^{10}Be and ^{26}Al depth profiles in Knyahinya (Leya & Masarik 2009). However, the modulation parameter $\Phi = 600$ MeV and with it the number of integral GCR particles of $J_{0,GCR} = 2.67$ cm^{-2} s^{-1} we used here are significantly different from the value of $\Phi = 500$ MeV and $J_{0,GCR} = 2.88$ cm^{-2} s^{-1} used in our earlier model (Leya & Masarik 2009). The difference is mostly due to the different particle spectra used for modeling, especially due to the differences in the low-energy region of the secondary proton spectra and the direct consideration of primary and secondary Galactic α particles (e.g., Hirtz 2019).

The recent study by Kim et al. (2010) using the MCNPX code was unable to simultaneously describe ^{10}Be and ^{26}Al depth profiles in the L-chondrite Knyahinya. If the modulation function, and with it the $J_{0,GCR}$ value, was chosen to describe the measured ^{26}Al depth profile, the ^{10}Be data were underestimated by 17% if MCNPX was using Bertini for the spallation part. The discrepancy increased to 25% if the Cascade-Exciton-Model (CEM) was used. The recent study by Argento et al. (2015a), which also used the MCNPX code system in combination with cross-section data for the relevant nuclear reactions, also fails to simultaneously describe the ^{10}Be and ^{26}Al depth profiles for Knyahinya. For ^{10}Be, the calculated data are lower than the measured data by ~60%; for ^{26}Al, the discrepancy is ~80%, i.e., for both nuclides, the discrepancy is significant.

To summarize, the comparison between modeled and experimental ^{10}Be and ^{26}Al data in Knyahinya indicates that the long-term average GCR spectrum at the meteoroid orbits, i.e., at ~3 au, can best be described using the solar modulation function $\Phi = 600$ MeV.

4.2. Elemental Production Rates

Figure 4 depicts the same modeled ^{10}Be and ^{26}Al depth profiles for the L-chondrite Knyahinya as shown before, again calculated by using a solar modulation function $\Phi = 600$ MV. However, here we distinguish contributions due to protons (dotted line), neutrons (dashed line), and α particles (dashed–dotted line). The largest contributions for both nuclides are due
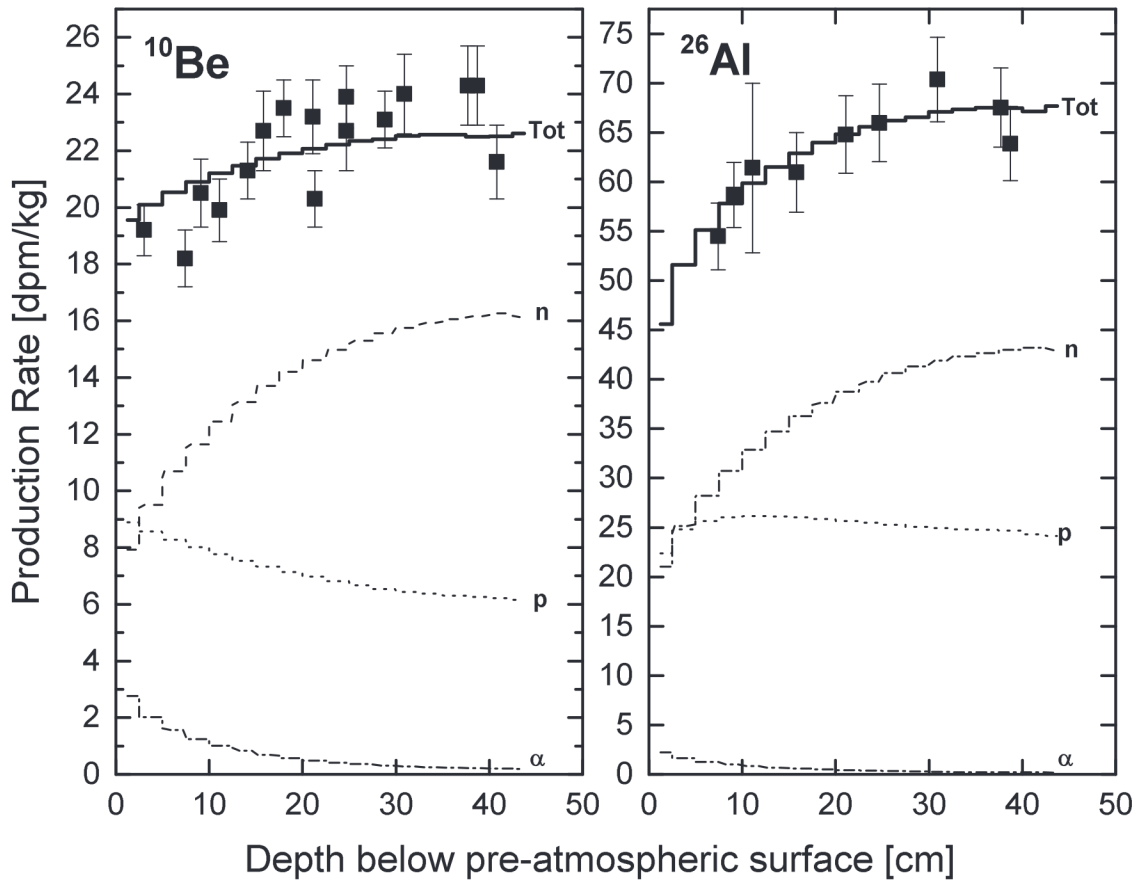
Figure 4. Depth profiles of ^{10}Be (left panel) and ^{26}Al (right panel) in the L-chondrite Knyahinya. The experimental data are from Graf et al. (1990b) renormalized to the changed AMS standards. For the model calculations, we use a solar modulation function $\Phi = 600$ MeV. For the depth profiles, the contributions due to protons (p), neutrons (n), and α particles (α) are distinguished.

to secondary neutrons. While the contributions for neutrons increase from the surface toward the center, the contributions for protons decrease from the surface toward the center. The same is true for α particles; their contributions also decrease from the surface toward the center.

The depth dependencies for the α-induced contributions for both nuclides are different from the depth dependencies for the proton- and neutron-induced contributions. Consequently, considering α particles directly, as it is done here for the very first time, changes the depth dependency of the total production rates. For the two nuclides shown here, the direct consideration of α particles makes the increase of the total production rates with increasing shielding depth less pronounced. With the α approximation, the depth profiles would look slightly different, i.e., they would increase more with depth.

4.3. Results for the Apollo 15 Drill Core—GCRs at 1 au

Based on the discussion in Section 2.3, we expect that the long-term average solar modulation function for the Earth and Moon at 1 au is slightly higher than the long-term average solar modulation function of $\Phi = 600$ MeV determined just above for the meteoroid orbits at ~3 au. To determine the Φ value at 1 au, we calculated the particle spectra for the Apollo 15 drill core using $\Phi = 564$ MeV (recent average determined by Usoskin et al. 2017; see also above), 620, 660, and 700 MeV. For modeling, we use the chemical composition of the Apollo 15 drill core (see Table 1) and for the density we assume $\rho = 1.76$ g cm^{-3}. The Apollo 15 drill core is well suited for

such a study because it is the least disturbed among all Apollo drill cores (Carrier 1974). To model the Moon, we use a spherical object with a radius of 1 km (see above), and we use 5×10^6 source particles to reach sufficient statistics.

The experimental data for ^{10}Be are from Nishiizumi et al. (1984a). The ^{10}Be data need no change despite the recent change of the accepted ^{10}Be half-life (see Nishiizumi et al. (2007)). For ^{26}Al, the experimental data are from Nishiizumi et al. (1984b) and Rancitelli et al. (1975). Unfortunately, for our studies, the experimental data scatter significantly, which makes the interpretation difficult. The comparison between measured and modeled ^{10}Be and ^{26}Al depth profiles for the Apollo 15 drill core is shown in Figure 5. First, it can be seen that all model results slightly overestimate the ^{10}Be and ^{26}Al data at depths larger than ~200 g cm^{-2}. For ^{10}Be, the overestimation, averaged for shielding depths larger than 200 g cm^{-2}, is 1.26, 1.20, 1.18, and 1.14 for $\Phi = 564$, 620, 660, and 700 MeV, respectively. For ^{26}Al, the model is too high by factors of 1.26, 1.21, 1.18, 1.15 for $\Phi = 564$, 620, 660, and 700 MeV, respectively. Second, at shallower depths, the results for $\Phi = 564$ and 620 MeV slightly overestimate the experimental data, indicating that the modulation function is slightly too low. In contrast, the model prediction for $\Phi = 700$ MeV is slightly too low, indicating a modulation function that is slightly too high. By quantifying the (depth-averaged) differences between modeled and experimental data and ignoring near-surface data due to SCR contributions, we calculated that a solar modulation function $\Phi = 660$ MeV
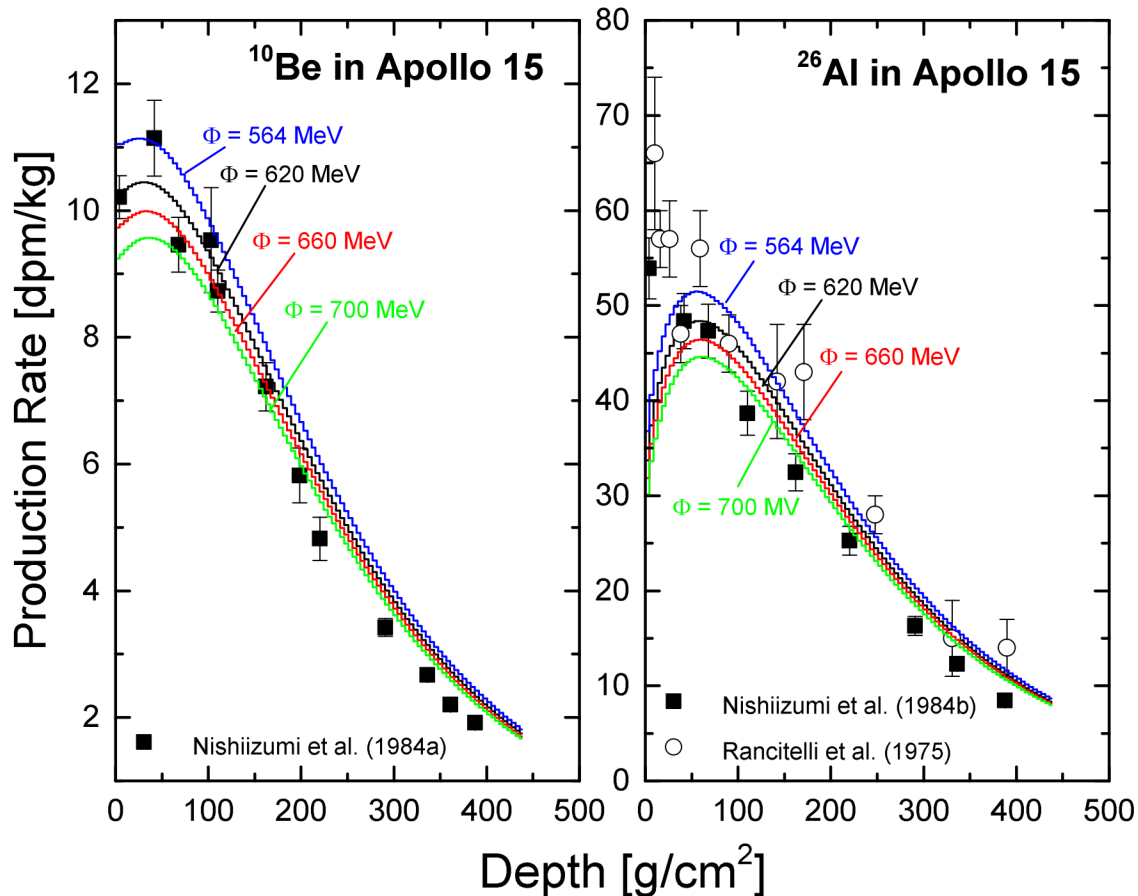
Figure 5. Depth profiles of ^{10}Be (left panel) and ^{26}Al (right panel) for the Apollo 15 lunar drill core. The experimental ^{10}Be data are from Nishiizumi et al. (1984a) and the ^{26}Al data are from Nishiizumi et al. (1984b) and Rancitelli et al. (1975). The depth profiles are for solar modulation functions of $\Phi = 564$ MeV (blue line), 620 MeV (black line), 660 MeV (red line), and 700 MeV (green line). The best agreement between model predictions and experimental ^{10}Be and ^{26}Al data is for a solar modulation function $\Phi \sim 660$ MeV.

describes the experimental ^{10}Be and ^{26}Al data best (red line in Figure 5). Third, the calculated ^{26}Al depth profiles are significantly lower than the experimental data at low shielding depths. This is due to contributions from solar cosmic rays, which are known to be relevant for ^{26}Al production at the Moon surface but which are not yet considered in our model. From the finding so far, we conclude that the long-term average solar modulation function for Earth and the Moon, i.e., for an orbital distance of 1 au, is ~660 MeV. Here it is worth emphasizing again that the solar modulation function we determined is a model-dependent parameter; it depends on the GCR spectrum and on the cross sections used for modeling.

A similar good agreement between experimental and modeled data has been obtained in the recent study by Li et al. (2017), also using the Geant4 toolkit. However, the authors used a different physics list, different cross sections, and a different parameterization for the GCR spectrum. Their calculations are based on a solar modulation function $\Phi = 550$ MeV, and they used the parameterization from Usoskin et al. (2005) for the GCR spectrum. Considering Equation (14), their value $\Phi = 550$ MeV corresponds to a solar modulation potential $\Phi = 455$ MeV for a GCR spectrum given by Castagnoli & Lal (1980), i.e., much lower than the value of $\Phi = 660$ MeV we used. The large difference in the solar modulation functions between the two approaches is likely due to the different physics lists used for Geant4 and the different cross sections used for modeling.

The study by Poluianov et al. (2018) only focused on ^{26}Al; ^{10}Be or other cosmogenic nuclides are not discussed. Also, by using the Geant4 code and experimental cross sections, the authors calculated ^{26}Al depth profiles for Apollo 15 samples for a variety of solar modulation potentials. The calculations are based on the LIS by Vos & Potgieter (2015) and the modulation approach summarized by Usoskin et al. (2017). According to their study, the best value for the long-term average solar modulation potential is $\Phi = 496 \pm 40$ MeV, again, significantly lower than the value we determined. However, if we compare the GCR spectrum with $\Phi = 660$ MeV from Castagnoli & Lal (1980) to a spectrum combining the LIS from Vos & Potgieter (2015) with the modulation part by Usoskin et al. (2017) using $\Phi = 496$ MeV, the differences in the modulated particle spectra are only very minor.

The study by Dong et al. (2014) used the Geant4 toolkit and the GCR spectrum given by Castagnoli & Lal (1980). Their results also describe the experimental data rather well but unfortunately, they give neither information on the physics list used nor on the solar modulation function used for modeling.

Finally, the study by Kim et al. (2010) based on the MCNPX code fails to simultaneously describe ^{10}Be and ^{26}Al depth profiles for the Apollo 15 drill core. If the spectrum was adjusted to describe the ^{10}Be depth profile, the ^{26}Al depth profile was 30% (using Bertini for the spallation part) or 40% (using CEM for the spallation part), too high compared to the

experimental data. In addition, the model is not in accord with the expected radial gradient, i.e., it fails to consistently and simultaneously describe cosmogenic nuclide production for the meteoroid orbits and at 1 au.

To summarize the results so far, we determined a long-term average solar modulation function at 1 au of $\Phi \sim 660$ MeV.

4.4. Long-term Average GCR Gradient as Determined from Cosmogenic Radionuclides

From our best estimates for the long-term average solar system modulation function of $\Phi = 600$ MeV for the meteoroid orbits at ~ 3 au and $\Phi = 660$ MeV for the Moon at 1 au, we can conclude that the long-term average gradient in the inner solar system is $\Delta\Phi \sim 30$ MeV au^{-1}. This corresponds to a gradient in the particle density of $\sim 5\%$ au^{-1}. This value agrees with the gradient of $4.5 \pm 0.5\%$ au^{-1} given by Gieseler et al. (2008). However, our finding is slightly lower than the (rather uncertain) gradient of $26 \pm 18\%$ au^{-1} determined by Alexeev et al. (2019) also by using cosmogenic nuclides (^{22}Na, ^{26}Al, ^{54}Mn). To calculate the gradient, the authors assumed that the long- and short-term variations in the GCR gradient are similar, which might not be the case. A gradient of 26% au^{-1} corresponds to a heliosphere of radius ~ 25 au, i.e., much too small. A possible explanation could be that the majority of the solar modulation gradient is in the inner solar system and that the gradient should become smaller at larger heliocentric distances. Unfortunately, with only two data points, one at 1 au and one at ~ 3 au, we cannot be more quantitative.

5. Long-term Changes of the Galactic Cosmic Rays and Constraints on Meteoroid Orbits

5.1. Were There Any Long-Term Changes in the Galactic Cosmic Rays?

Figure 5 demonstrates that the ^{10}Be and ^{26}Al depth profiles calculated for the Apollo 15 drill core using a solar modulation function $\Phi = 564$ MeV, which is the average solar modulation function at 1 au for the years 1951 to 2005 (Usoskin et al. 2005, normalized to CL80, see above), gives a bad description of the experimental data. Our best estimate for the long-term (3–4 Myr) average solar modulation function at 1 au is ~ 660 MeV. Consequently, we can conclude that the recent average solar modulation function for the years 1951–2005 is significantly different from the long-term average over the last ~ 3–4 million years (2–3 half-lives of ^{10}Be and ^{26}Al). To be slightly more quantitative, a spectrum as given by Castagnoli & Lal (1980) with $\Phi = 660$ MeV corresponds to a primary proton flux of 2.41 cm^{-2} s^{-1}. On the other hand, a spectrum with $\Phi = 564$ MV corresponds to 2.85 cm^{-2} s^{-1}, which is 18% higher than the long-term average. Consequently, the data for the Apollo 15 drill core indicate that the long-term GCR flux at 1 au was $\sim 20\%$ lower than the recent average since 1951.

Interestingly, Vahia (2004, 2006) studied changes of the heliopause due to changing conditions of the local ISM and proposed that the current flux (back to 10^4 yr before present (BP)) of GCR particles with energies larger than 100 MeV was higher than the flux in the time period 10^4 yr BP–10^5 yr BP. During this time period, the solar system was in a bubble of the local ISM. Furthermore, he proposed that the flux from 10^5 to 10^7 yr BP, i.e., the flux relevant for ^{10}Be and ^{26}Al production, was much higher than any other flux before or after. During this time period, the solar system was in an interarm region.

Consequently, according to this study, the current GCR flux should be lower than the long-term average relevant for ^{10}Be and ^{26}Al production, in contrast to what we found. However, one could also turn the entire discussion of this study around and argue that the GCR flux density in interarm regions should be lower than the average, which would argue for lower flux densities in the time period 10^5–10^7 yr, in contrast to the study by Vahia (2004, 2006) but in agreement with what we found.

Another possibility that has been proposed for studying temporal changes in the GCR intensity and the solar modulation function is via the ^{22}Na/^{26}Al production rate ratios in solar system objects. The rationale is as follows: for the same solar modulation function, the production rate ratio ^{22}Na/^{26}Al is almost insensitive to the size of the irradiated object, the depth within this object, and its chemical composition. In contrast, while the cosmogenic ^{26}Al production rate depends on the average GCR intensity (solar modulation function) over the last ~ 1.5 Myr (~ 2 half-lives of ^{26}Al), the ^{22}Na production rate reflects only the GCR intensity and the solar modulation function for the last ~ 5 yr (~ 2 half-lives of ^{22}Na). Consequently, variations in the ^{22}Na/^{26}Al production rate ratio cannot be due to variations in radius, depth, or chemical composition but must be due to GCR intensity variations, which enable us to study whether the GCR intensity for the last ~ 5 yr was similar to the average GCR intensity (solar modulation function) for the last ~ 3–4 Myr.

For this purpose, we calculated the ^{22}Na and ^{26}Al production rates for the Apollo 15 drill core. The model calculations for ^{26}Al are based on a solar modulation function $\Phi = 660$ MeV, which we determined above to be the average solar modulation function for the last few million years. For ^{22}Na, we performed model calculations using $\Phi = 564$ MeV, 620 MV, 660 MeV, and 700 MeV. The ^{22}Na/^{26}Al production rate ratios measured in Apollo 15 samples reflect the solar modulation during the five years before the Apollo 15 mission, i.e., from 1966 to 1971, relative to the long-term average. From the data by Usoskin et al. (2017), normalized to CL80 and shown in Figure 2, we calculate an average solar modulation function $\Phi \sim 605$ MeV for the years 1966–1971. In a diagram of ^{22}Na production rates as a function of ^{26}Al production rates, the slope depends on the solar modulation functions relevant for ^{22}Na production relative to the long-term average relevant for ^{26}Al production. For example, if both nuclides are produced under the same solar modulation, the data would plot on a certain slope (in our case, the slope for $\Phi = 660$ MeV). In contrast, if ^{22}Na are produced at a higher (lower) solar modulation than ^{26}Al, the slope would become lower (higher). In this diagram, effects due to solar cosmic rays and gardening are ignored. The modeled results are shown in Figure 6 (left panel). Considering the data from Rancitelli et al. (1975) for the Apollo 15 drill core, there is a reasonable agreement between the experimental data and the model predictions. However, the experimental data scatter too much to discern a real trend. The model calculations also indicate that the ^{22}Na/^{26}Al production rate ratio does not vary enough to be really useful for studies of long-term changes of the solar modulation function, at least not in the range $\Phi = 564$–700 MeV we studied. To be more quantitative, the average ^{22}Na/^{26}Al production rate ratios calculated for the Apollo 15 drill core and for $\Phi = 564$ MeV, 620 MeV, 660 MeV, and 700 MeV are 0.85 ± 0.06, 0.81 ± 0.05, 0.78 ± 0.04, 0.76 ± 0.03, respectively, i.e., the variability is only 11% for the studied range of solar modulation functions.
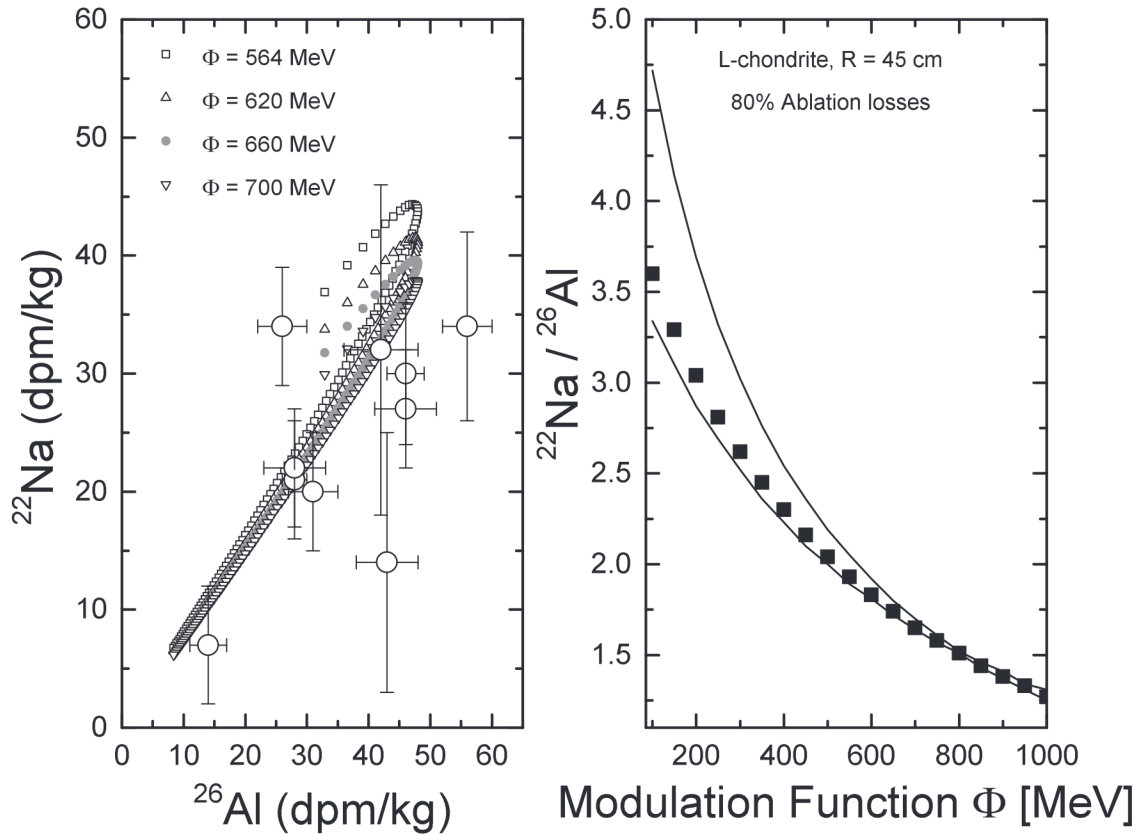
Figure 6. ^{22}Na as a function of ^{26}Al for Apollo 15 drill core samples. The model calculations for ^{22}Na are for the solar modulation functions $\Phi = 564$, 620, 660, and 700 MeV and the model calculation for ^{26}Al is always for $\Phi = 660$ MeV. The experimental data are from Rancitelli et al. (1975; left panel). ^{22}Na/^{26}Al production rate ratios in L-chondrites with a preatmospheric radius of 45 cm. The given points are weighted averages assuming ∼80% ablation losses. The solar modulation function varying from $\Phi = 100$ MeV to $\Phi = 1000$ MeV is for ^{22}Na; the ^{26}Al production rates are always for $\Phi = 600$ MeV. The upper and lower curves represent the maximum and minimum ratios, respectively. For more information see text (right panel).

Next, we discuss the variability of ^{22}Na/^{26}Al production rate ratios for an L-chondrite with a preatmospheric radius of 45 cm, i.e., for an average orbit of ∼3 au. Doing so, we use the ^{26}Al production rates for an L-chondrite having a preatmospheric radius of 45 cm calculated using a solar modulation function $\Phi = 600$ MeV, i.e., corresponding to the long-term average for the meteoroid orbits as determined above (see Section 4.1). For ^{22}Na, we use the same object, an L-chondrite with a preatmospheric radius of 45 cm, but we varied the solar modulation function from $\Phi = 100$ MeV to $\Phi = 1000$ MeV in steps of $\Delta\Phi = 50$ MeV. The range of possible ratios has been reduced by assuming ∼80% ablation losses (Bhandari et al. 1980), i.e., by considering only the innermost 25 cm of the 45 cm object. From this data, we calculated weighted averages, using the mass of the individual shells as weights. This finally gives a weighted average ^{22}Na/^{26}Al production rate ratio for each solar modulation function; shown as solid symbols in Figure 6 (right panel). The upper and lower limits are shown by the two solid lines. The correlation between ^{22}Na/^{26}Al and solar modulation function can be fitted via

$$P(^{22}\text{Na})/P(^{26}\text{Al}) = 0.918 + 2.696 \times e^{\frac{-(\Phi - 92.09)}{462.02}}. \quad (18)$$

Because Equation (18) is only for L-chondrites with a preatmospheric radius of 45 cm, the following discussion is biased accordingly. In an experimental study, Evans et al. (1982) measured ^{22}Na/^{26}Al production rate ratios in 47 samples from 24 meteorite falls. The measured ratios range

between 1.04 ± 0.05 for the meteorite Malakal and 4.56 ± 0.38 for the meteorite Jilin. The ratio for Jilin is not representative because this meteorite experienced a complex exposure history and ^{26}Al is not in saturation, making the ^{22}Na/^{26}Al ratio too high (Begemann et al. 1985). Ignoring Jilin for the discussion, the upper limit is reduced to 2.48 for the meteorite Dhajala. Again, excluding Jilin, the average value for the ^{22}Na/^{26}Al ratio for the studied meteorites is 1.46 ± 0.27. Both the range and the average value are in agreement with the model predictions. In addition, the ^{22}Na/^{26}Al ratios for a variety of ordinary chondrites studied by Bhandari et al. (1994) range between ∼1 and ∼2.3, again in agreement with the model predictions. For the meteorite Chelyabinsk, Alexeev et al. (2019) give ^{22}Na/^{26}Al ratios of 1.4 ± 1.2 for a depth larger than 100 cm, 2.42 ± 0.17 at a depth of 10–50 cm, and of 2.53 ± 0.24 for depths of 50–100 cm. For the Košice meteorite, the same authors measured 1.45 ± 0.20 for depths below 10 cm and 1.52 ± 0.21 for depths between 10 and 50 cm. All values are well within the range of the predicted ^{22}Na/^{26}Al ratios we modeled for an L-chondrite with a radius of 45 cm (see Figure 6).

The data for meteorites indicate that the ^{22}Na/^{26}Al production rate ratios vary enough to be useful for studies on the temporal variability of the solar modulation function. For the following, more qualitative discussion, we use the reconstruction of the solar modulation function given by Usoskin et al. (2017) shown in Figure 2. Because the data are

for 1 au, we adjusted them to the meteoroid orbits at ∼3 au by simply subtracting $\Delta\Phi = 60$ MeV, which we determined above as the best value for the long-term average gradient in the inner solar system (see also Section 2.3). Note that this procedure is surely not entirely correct because the radial gradient in the inner solar system is expected to vary on short timescales. However, for our qualitative discussion, this rough assumption is sufficient. Considering now a meteorite that fell in 1970, the ^{22}Na production rate is determined by the solar modulation function from ∼1965 to ∼1970, which was $\langle\Phi\rangle \sim 480$ MeV. According to Equation (18), this corresponds to a ^{22}Na/^{26}Al (1965–1970) production rate ratio of ∼2.08. For a meteorite that fell in 1980, the relevant parameters are $\langle\Phi\rangle \sim 420$ MeV and ^{22}Na/^{26}Al (1975–1980) ∼2.25. Finally, a meteorite that fell in 1985 experienced $\langle\Phi\rangle \sim 670$ MeV, corresponding to ^{22}Na/^{26}Al (1980–1985) ∼1.7. Consequently, the variability in ^{22}Na/^{26}Al production rate ratios for the three cases is more than 30%, sufficient for detailed studies of the temporal variability of the solar modulation function using freshly fallen meteorites.

5.2. Can We Put Constraints on the Meteoroid Orbits?

For the qualitative discussion above, we assumed that the meteorites spent their entire lifetime in the same orbit at ∼3 au and that the transfer from the asteroid belt to Earth was almost instantaneous. This assumption is not entirely correct. Indeed, the meteorites spent most of their lifetime in the asteroid belt but at one point they are ejected, likely from the so-called Kirkwood gaps caused by orbital resonances with Jupiter. Subsequently, the meteorites will develop more elliptical orbits and will spend a substantial amount of their travel time in the inner solar system, i.e., at higher solar modulation functions. In this picture, the ^{26}Al production rate is governed by the solar modulation in the asteroid belt but ^{22}Na is governed by the solar modulation shortly before the fall in the inner solar system. Consequently, the ^{22}Na/^{26}Al production rate ratios can also be used to better constrain the final orbit of a meteorite shortly before its fall, or at least the ratio can confirm or reject the orbit estimated based on observations and/or photos.

As an example, we discuss the data for the H5 chondrite Lost City that fell in 1970. The ^{22}Na/^{26}Al production rate ratios range from 1.24 ± 0.18 to 1.58 ± 0.10; the average ratio is 1.37 ± 0.05 (Evans et al. 1982). According to Equation (18), this ratio corresponds to a solar modulation function $\Phi \sim 920$ MeV. Going back to the data from Usoskin et al. (2017), the average modulation function at 1 au for the time period 1967–1969 was ∼640 ± 60 MeV, i.e., significantly lower. For $\Phi = 640$ MeV, we would expect a ^{22}Na/^{26}Al production rate ratio of ∼1.74, i.e., higher than the experimental ratio. Consequently, comparing model predictions and experimental data indicates that most of the ^{22}Na production was at a high solar modulation function, higher than expected for orbits at 3 au but also higher than expected for orbits at 1 au at this time. A reasonable assumption therefore would be that the orbit of Lost City before its fall on Earth was relatively close to the Sun, i.e., much closer than 1 au, and that there was a large radial gradient in the inner solar system. For example, assuming $\Phi \sim 660$ MeV at 1 au and with $\Phi \sim 920$ MV needed to explain the ^{22}Na/^{26}Al ratios for Lost City, we calculate a drop in the GCR flux density of ∼65%, which corresponds to a radial gradient larger than ∼65% au^{-1}. In addition, we could also argue that some parts of the Lost City orbit were above or below the ecliptic, corresponding to lower GCR intensities and higher gradients.

For the meteorites Košice and Chelyabinsk, the average ^{22}Na/^{26}Al ratios are 1.49 and 2.48, respectively, which is surprisingly different considering that both meteorites fell only ∼3 yr apart (Alexeev et al. 2019). However, ^{26}Al in Chelyabinsk is not in saturation due to the short cosmic-ray exposure age of ∼1.2 Ma (Nishiizumi et al. 2013; Alexeev et al. 2019). Correcting the ^{26}Al data for undersaturation reduces the ^{22}Na/^{26}Al ratio to ∼1.7, i.e., in better agreement to the data for Košice. Here we focus on the data for Košice; the ^{22}Na/^{26}Al ratio of 1.49 corresponds to $\Phi \sim 810$ MeV. This high value is somewhat surprising considering that Košice fell close to the minimum of solar activity during the 23rd solar cycle. Again, the data indicate that the final part of the meteorite orbit was most likely very close to the Sun and was governed by low GCR intensities.

Remember that the discussion is significantly biased because Equation (18) is only valid for L-chondrites with a preatmospheric radius of 45 cm. In contrast, Lost City is an H5 chondrite that was most likely smaller, Chelyabinsk is an LL5 chondrite that was much larger. Košice is an H5 chondrite that was likely smaller than 45 cm. Another limitation is that we are currently not considering any uncertainties. Consequently, the discussion above is only qualitative and is just to demonstrate that a combination of short- and long-lived cosmogenic nuclides in meteorites or the lunar surface can be used to study the temporal variability and the radial gradient of the GCR flux and the solar modulation function.

6. Conclusions

Here we present the first results of our new generation of model calculations, i.e., version V03. The model is based on improved and very sophisticated Monte Carlo calculations for particle transport. The Geant4 toolkit used is using the latest and most reliable approach for the intranuclear cascade, called INCL++6. Thanks to the recent improvements (extending the code to lower and higher energies, considering light charged particles as ejectiles and projectiles), we can for the first time directly consider primary and secondary Galactic α particles. In addition to the improved particle spectra, we also reinvestigated some of the cross sections, which was necessary due to recent changes in accepted half-lives and/or changes in AMS standards.

Here we present the first results, i.e., ^{10}Be and ^{26}Al depth profiles for an L-chondrite with a preatmospheric radius of 45 cm, which is a good proxy for the very well-studied meteorite Knyahinya. By comparing measured and modeled depth profiles, we concluded that the long-term average solar modulation function, which is a proxy for the GCR intensity, was $\Phi = 600$ MeV. This is our best estimate for the long-term average solar modulation potential at the meteoroid orbit, i.e., at ∼3 au.

We also calculated the ^{10}Be and ^{26}Al depth profiles for the Apollo 15 drill core for determining the long-term average solar modulation function at 1 au. Our best estimate is $\Phi = 660$ MeV. From the finding, we calculate a long-term average gradient for the solar modulation function of $\Delta\Phi = 30$ MeV au^{-1}, which corresponds to a gradient for the GCR intensity of ∼5% au^{-1}. Our result is in very good agreement with the gradients found in studies based on space mission data.

By extending the model to the short-lived radionuclide ^{22}Na, we elaborate on the possibilities to study temporal GCR intensity variations using ^{22}Na/^{26}Al production rate ratios. The ^{22}Na/^{26}Al production rate ratio in lunar samples is not a good measure for the temporal variation of the solar modulation function Φ. First, the uncertainties of the experimental data are very large, preventing us from seeing any trend. Second, even with lower uncertainties, the ratio does not vary enough with solar modulation to be useful. For meteorites, in contrast, the ^{22}Na/^{26}Al production rate ratio varies by almost a factor of $\sim$3, which would be sufficient for more detailed studies on temporal GCR intensity variations. We also elaborated briefly on the possibility of putting some constraints on the meteoroid orbits shortly before their fall. However, the study so far is seriously limited because it is based only on the model calculations for an L-chondrite with a preatmospheric radius of 45 cm.

ORCID iDs

Ingo Leya ⬤ https://orcid.org/0000-0002-3843-6681

References

Abe, K., Fuke, H., Haino, S., et al. 2016, ApJ, 822, 65
Agostinelli, S., Allison, J., Amako, K., et al. 2003, NIMPA, 506, 250
Alexeev, V. A., Laubenstein, M., Povinec, P. P., & Ustinova, G. K. 2019, SoSyR, 53, 97
Amato, E., & Blasi, P. 2018, AdSpR, 62, 2731
Ammon, K., Masarik, J., & Leya, I. 2008, M&PS, 44, 485
Argento, D. C., Stone, J. O., Reedy, R. C., & O'Brian, K. 2015a, Quat. Geochron., 26, 29
Argento, D. C., Stone, J. O., Reedy, R. C., & O'Brian, K. 2015b, Quat. Geochron., 26, 44
Baade, W., & Zwicky, F. 1934a, PNAS, 20, 254
Baade, W., & Zwicky, F. 1934b, PNAS, 20, 259
Baade, W., & Zwicky, F. 1934c, PhRv, 46, 76
Begemann, F., Si, Z., Schmitt-Strecker, S., Weber, H. W., & Xu, Z. 1985, E&PSL, 72, 247
Bhandari, N., Bonino, G., Castagnoli, G. C., & Taricco, C. 1994, Metic, 29, 443
Bhandari, N., Lal, D., Nautiyal, C. M., et al. 1980, Metic, 15, 265
Binns, W. R., Wiedenbeck, M. E., Arnould, M., et al. 2008, ApJ, 634, 351
Boshini, M. J., Della Torre, S., Gervasi, M., et al. 2020, ApJS, 250, 27
Boshini, M. J., Della Torre, S., Gervasi, M., La Vacca, G., & Rancoita, P. G. 2018, AdSpR, 62, 2859
Burger, R. A., Potgieter, M. S., & Heber, B. 2000, JGR, 105, 27447
Caballero-Lopez, R., & Moraal, H. 2004, JGRA, 109, A01101
Carrier, W. D., III 1974, Moon, 11, 183
Castagnoli, G. C., & Lal, D. 1980, Radiocarbon, 22, 133
Chmeleff, J., von Blanckenburg, F., Kossert, K., & Jakob, D. 2010, NIMPB, 268, 192
Christl, M., Vockenhuber, C., Kubik, P. W., et al. 2013, NIMPB, 294, 29
David, J. C. 2015, EPJA, 51, 68
David, J.-C., & Leya, I. 2019, PrPNP, 109, 103711
De Simone, N., Di Felice, V., Gieseler, J., et al. 2011, ASTRA, 7, 425
Della Torre, S., Gervasi, M., Grandi, D., et al. 2016, in XXV European Cosmic Ray Symp., ed. L. Castellie, C16-09-04.3
Dong, T.-K., Yun, S.-J., Ma, T., et al. 2014, ChPhC, 38, 075101
Evans, J. C., Reeves, J. H., Rancitelli, L. A., & Bogard, D. D. 1982, JGR, 87, 5577
Florinski, V., Ferreira, S. E. S., & Pogorelov, N. V. 2013, SSRv, 176, 147
Forman, M. A., & Schaeffer, O. A. 1979, RvGSP, 17, 556
Fujii, Z., & McDonald, B. 1997, JGR, 102, 24201

Garcia-Munoz, M., Mason, G. M., & Simpson, J. A. 1975, ApJ, 2002, 265
Gieseler, J., Heber, B., Dunzlaff, P., et al. 2008, ICRC (Mérida), 30, 571
Gold, T., Bilson, E., Baron, R. L., Ali, M. Z., & Ehmann, W. D. 1977, LPSC, 8, 3633
Graf, Th., Baur, H., & Signer, P. 1990a, GeCoA, 54, 2521
Graf, Th., Signer, P., Wieler, R., et al. 1990b, GeCoA, 54, 2511
Herbst, K., Kopp, A., Heber, B., et al. 2010, JGRA, 115, D00120
Hess, V. F. 1912, PhyZ, 13, 1084
Hirtz, J. 2019, PhD thesis, Univ. Bern
Hirtz, J., David, J.-C., Boudard, A., et al. 2018, EPJP, 1332, 436
Hirtz, J., David, J.-C., Boudard, A., et al. 2020, PhRvC, 101, 014608
Kim, K. J., Masarik, J., & Reedy, R. C. 2010, NIMPB, 268, 1291
Kohlhörster, W. 1913, PhyZ, 14, 1153
Kohlhörster, W. 1914, Verh. Deut. Phys. Ges., 16, 719
Koning, A. J., & Rochman, D. 2012, NDS, 113, 2841
Langner, U. W., Potgieter, M. S., & Webber, W. R. 2003, JGRA, 108, 8039
Leray, S., Mancusi, D., Kaitaniemi, P., et al. 2013, JPhCS, 420, 012065
Leya, I., & Masarik, J. 2009, M&PS, 44, 1061
Leya, I., & Michel, R. 2011, NIMPB, 269, 2487
Li, Y., Zhang, X., Dong, W., et al. 2017, JGRA, 122, 1473
Lingenfelter, R. E. 2018, AdSpR, 62, 2750
Mancusi, D., Boudard, A., Cugnon, J., et al. 2014, PhRvC, 90, 054602
Marquard, J., & Heber, B. 2019, A&A, 625, A153
Masarik, J., & Beer, J. 1999, JGR, 114, 12099
Masarik, J., & Reedy, R. C. 1996, JGR, 101, 18891
Mason, B., & Wiik, H. B. 1963, Am. Mus. Novitates, 2154, 1
McDonald, F. B., Fujii, Z., & Lal, N. 2003, AdSpR, 32, 633
McKibben, R. B. 1975, RvGSP, 13, 1088
McKinney, G. W., Lawrence, D. J., Prettyman, T. H., et al. 2006, JGRE, 111, E06004
Michel, R., Hansmann, D., Glasser, W., et al. 2015, NIMPB, 343, 30
Morales-Olivares, O. G., & Caballero-López, R. A. 2009, GeofI, 48, 237
Moskalenko, I. V., Strong, A. W., Ormes, J. F., & Potgieter, M. S. 2002, ApJ, 565, 280
Ngobeni, M. D., & Potgieter, M. S. 2011, AdSpR, 48, 1480
Ngobeni, M. D., & Potgieter, M. S. 2012, AdSpR, 49, 1660
Nishiizumi, K., Caffee, M. W., Huber, L., Welten, K. C., & Wieler, R. 2013, in 76th Annual Meteoritical Society Meeting, 5260
Nishiizumi, K., Elmore, D., Ma, X. Z., & Arnold, J. R. 1984a, E&PSL, 70, 157
Nishiizumi, K., Imamura, M., Caffee, M. W., et al. 2007, NIMPB, 258, 403
Nishiizumi, K., Klein, J., Middleton, R., & Arnold, J. R. 1984b, E&PSL, 70, 164
Parker, E. N. 1965, P&SS, 13, 9
Poluianov, S., Kovaltsov, G. A., & Usoskin, I. G. 2018, A&A, 518, A96
Potgieter, M. S. 2013, LRSP, 10, 3
Rancitelli, L. A., Fruchter, J. S., Felix, W. D., Perkins, R. W., & Wogman, N. A. 1975, LPSC, 6, 1891
Scherer, K., Fichtner, H., & Borrmann, T. 2006, SSRv, 127, 327
Serber, R. 1947, PhRv, 72, 1114
Shaviv, N. J. 2002, PhRvL, 89, 051102
Shaviv, N. J. 2003, NewA, 8, 39
Simpson, J. A. 1983, in Proc. Advanced Study Institute: Composition and Origin of Cosmic Rays (Dordrecht: D. Reidel), 1
Sloan, T., & Wolfendale, A. W. 2013, NewA, 25, 45
Steinhilber, F., Abreu, J. A., & Beer, J. 2008, ASTRA, 4, 1
Stone, E. C., Cummings, A. C., Heikkila, B. C., & Lal, N. 2019, NatAs, 3, 1013
Stone, E. C., Cummings, A. C., McDonald, F. B., et al. 2013, Sci, 341, 150
Ushinsky, V. 2010, in Joint Int. Conf. on Supercomputing in Nuclear Applications and Monte Carlo 2010, 17
Usoskin, I. G., Alanko-Huatari, K., Kovaltsov, G. A., & Mursula, K. 2005, JGRA, 110, A12108
Usoskin, I. G., Gil, A., Kovaltsov, G. A., Mishev, A. L., & Mikhailov, V. V. 2017, JGRA, 122, 3875
Vahia, M. N. 2004, arXiv:astro-ph/0404081
Vahia, M. N. 2006, in Proc. ILWS Workshop, ed. N. Gopalswamy & A. Bhattacharyya, 189
Vonmoos, M., Beer, J., & Muscheler, R. 2006, JGRA, 111, A10105
Vos, E. E., & Potgieter, M. S. 2015, ApJ, 851, 119
Walker, F., Axford, I., & Wood, D. 1985, ICRC (San Diego), 5, 189
Walter, M., & Wolfendale, A. W. 2012, EPJH, 37, 323
Webber, H. R., & Higbie, P. R. 2003, JGRA, 108, 1355
Webber, W. R., & Higbie, P. R. 2009, JGRA, 114, A02103
Webber, W. R., & McDonald, F. B. 2013, GeoRL, 40, 1665
Zhang, M., & Pogorelov, N. 2000, ApJ, 895, 1